JGR Oceans

RESEARCH ARTICLE
10.1029/2024JC020957

What Can Hurricane Sam (2021) Tell Us About Extreme Ocean Waves Under Tropical Cyclones?

X. Zhao[1,2], L. Oruba[2], D. Hauser[2], B. Zhang[1], and E. Dormy[3]

[1]School of Marine Sciences, Nanjing University of Information Science and Technology, Nanjing, China, [2]Laboratoire Atmosphères, Observations Spatiales (LATMOS), Sorbonne Université, UVSQ, CNRS, Paris, France, [3]Département de Mathématiques et Applications, Ecole Normale Supérieure, CNRS, PSL University, Paris, France

Abstract We investigate the ocean wave field under Hurricane Sam (2021). Whilst measurements of waves under Tropical Cyclones are rare, an unusually large number of quality in situ and remote measurements are available in that case. First, we highlight the good consistency between the wave spectra provided by the Surface Waves Investigation and Monitoring (SWIM) instrument onboard the China-France Oceanography SATellite, the in situ spectra measured by National Data Buoy Center buoys, and a saildrone. The impact of strong rains on SWIM spectra is then further investigated. We show that whereas the rain definitely affects the normalized radar cross section, both the innovative technology (beam rotating scanning geometry) and the post-processing processes applied to retrieve the 2D wave spectra ensure a good quality of the resulting wave spectra, even in heavy rain conditions. On this basis, the satellite, airborne and in situ observations are confronted to the analytical model proposed by Kudryavtsev et al. (2015, https://doi.org/10.1002/2015JC011284). We show that an extended fetch mechanism may be invoked to explain the large significant wave height observed in the right front quadrant of Hurricane Sam.

Plain Language Summary Wave measurements in Tropical Cyclones can be performed by radars onboard satellites or aircrafts, and by in situ devices such as buoys or saildrones. In 2021, a saildrone sailed in Hurricane Sam, providing the first video images of extreme weather in a hurricane, as well as wind and wave measurements. Hurricane Sam was also monitored by the Surface Waves Investigation and Monitoring instrument onboard the China-France Oceanography SATellite, which measures the wave energy distribution. We explain why these measurements are reliable, despite the heavy rain conditions. Combining all observational data available for Hurricane Sam, we show that the most extreme waves are consistent with the so-called extended-fetch mechanism, whereby waves traveling at a velocity similar to the TC displacement can undergo a phenomenal growth.

Key Points:

- We take advantage of the unusually large number of observations in Hurricane Sam (2021) to study the physics of waves under a hurricane
- The innovative China-France Oceanography SATellite-Surface Waves Investigation and Monitoring instrument provides 2D wave spectra which are reliable despite the heavy rain conditions in hurricanes
- The trapped wave mechanism, or extended fetch, scenario can be successfully compared with observations by a saildrone and a National Data Buoy Center buoy

Supporting Information:

Supporting Information may be found in the online version of this article.

Correspondence to:

L. Oruba,
ludivine.oruba@latmos.ipsl.fr

Citation:

Zhao, X., Oruba, L., Hauser, D., Zhang, B., & Dormy, E. (2024). What can Hurricane Sam (2021) tell us about extreme ocean waves under tropical cyclones? *Journal of Geophysical Research: Oceans*, *129*, e2024JC020957. https://doi.org/10.1029/2024JC020957

Received 25 JAN 2024
Accepted 31 JUL 2024

Author Contributions:

Data curation: X. Zhao
Funding acquisition: L. Oruba, B. Zhang, E. Dormy
Investigation: X. Zhao, L. Oruba, E. Dormy
Methodology: L. Oruba, E. Dormy
Software: X. Zhao
Supervision: L. Oruba
Validation: B. Zhang
Visualization: X. Zhao
Writing – original draft: L. Oruba, E. Dormy

1. Introduction

Ocean wave measurements under Tropical Cyclones (TCs) are essential to improve our understanding of the generation of waves by TCs. They are unfortunately relatively rare and the reliability of the few existing measurements is often questioned because of the extreme wind and rain conditions inside TCs.

Gravity waves induced by the wind blowing at the surface of the ocean can be measured by in situ devices or by radars onboard aircrafts or satellites. The network of the National Data Buoy Center (NDBC) provides measurements of the Significant Wave Height (SWH), their wavelength and their direction of propagation, as well as measurements of the surface wind. They are a valuable part of the US hurricane warning system and also provide precious observations for research. In 2021, the National Oceanic and Atmospheric Administration (NOAA) and the Saildrone US company have deployed 5 explorer uncrewed surface vehicles designed to make measurements of physical parameters, including waves, within hurricanes, between July and October 2021. On 30 September, one of the saildrones (SDs), SD 1045, crossed Hurricane Sam, on which the present article is focused, and provided the first video of extreme conditions in a major hurricane.

Since 2019, the Chinese-French Oceanography SATellite (CFOSAT) provides directional wave spectra at the global scale thanks to a rotating multi-beam radar called SWIM (Surface Waves Investigation and Monitoring). These spectra cover the wavelength range [70–500] m, giving access to both the wind-sea and the swell waves (Hauser et al., 2021). So far, wave measurements were performed by satellite radar altimeters, providing a global coverage of significant wave height, and by Synthetic Aperture Radars (SAR) onboard satellites (e.g., Sentinel),

Writing – review & editing: D. Hauser, E. Dormy

providing two-dimensional spectra. These spectra are however limited by the so-called azimuth cut-off effect which prevents measurements of the wind sea waves or short swell propagating in directions close to the azimuth direction (see Hauser et al., 2023, for a review). The CFOSAT-SWIM provides an unprecedented detailed description of the waves, offering a chance to measure the wind sea waves. A finer estimate of these waves is crucial for the investigation of wind-waves generated by extreme events like TCs (e.g., Oruba et al., 2022). The CFOSAT satellite also carries a SCATterometer (CSCAT) providing surface wind measurements, collocated with the wave measurements by SWIM. Since 2008, directional wave spectra are also provided by the NOAA Wide Swath Radar Altimeter (WSRA) aboard hurricane reconnaissance aircrafts. Several reconnaissance flights were operated by the NOAA in the case of Hurricane Sam.

The impact of rain on satellite wind and wave products is a major issue. The electromagnetic waves are attenuated and scattered by the atmosphere, mainly due to the presence of water vapor and liquid water (clouds and rain), high frequencies (X-Ku-K-Ka bands) being more impacted than low frequencies (C-S-L bands). Moreover, it is known that raindrops impinging onto the sea surface modifies the short waves and impacts the wave growth in a very complex way (Cavaleri et al., 2015). Jointly with the effect of atmospheric attenuation, the modification of short waves affects the radar backscatter signals. Quilfen et al. (2006, 2010) have however shown that, using dual-frequency altimeters, operating at both C and Ku band microwave frequencies, reliable estimates of wind speed and rain rate can be obtained in tropical cyclones. As for SWH, which is retrieved from the shape of the returned signal waveform, the impact of rain has not been extensively studied yet. However, Tournadre et al. (2009) show, from simulations applied to Ka-Band radar signals, that SWH is little affected by rain. Concerning SAR observations in C-band, Alpers et al. (2016) have shown the important and complex impact of rain on the normalized radar cross sections at medium incidence, whereas Zhao et al. (2021) have analyzed more specifically the impact of rain on wave spectra retrieved in tropical cyclones. The results of Zhao et al. (2021) show an important impact of rain on the accuracy of the retrieved SWH at all the studied incidences (from about 20° to about 50°). They also show that due to the rain impact, the shape of the wave spectra estimated from observations at medium incidence angles (around 40°) depart significantly from their reference spectra.

The rain impact on SWIM measurements (performed in the Ku band) has, so far, not been investigated. However, SWIM products have been used in several studies on the wave field in TCs. Among them, Yurovskaya et al. (2022) analyzed the tropical cyclone Goni (2020) by combining multi-satellite observations (including SWIM wave spectra) and a 2D parametric wave model. Other studies are based on a statistical approach, using data over one to several years at the global scale. Xiang et al. (2022) performed a quantitative comparison of the SWIM and CSCAT measurements in TCs to other satellite measurements and model outputs, whereas Shi et al. (2021) and Le Merle et al. (2022) investigated the wave distribution in TCs. Shi et al. (2021) highlighted the SWH asymmetry in TCs, with the highest waves on the right of the TC track in the Northern Hemisphere (on the left in the Southern Hemisphere). The SWH's asymmetry was also shown to mainly depend on the TC intensity, with SWH asymmetry decreasing with TC intensification. Using 3 years of SWIM data in the Northern Hemisphere, Le Merle et al. (2022) performed an analysis of the wave characteristics in 67 TCs, by classifying them in three categories (slow, moderate and fast speed), depending on the ratio between the maximum sustained wind and the displacement velocity. The highest SWHs were found in the left-front quadrant for slow-moving TCs, in the right-front quadrant for moderate speed TCs and in the right-rear quadrant for fast-moving TCs.

More generally, the wave field in tropical and extra-tropical cyclones has been investigated in several studies (see Young, 2017 for a review on tropical cyclones and Ponce de León & Bettencourt, 2021 on extra-tropical cyclones). It has been noted that the SWH's asymmetry could partly result from the asymmetry of the wind field. However, an other mechanism provides an additional, perhaps even more important, source of asymmetry. The "wave containment" phenomenon has been discussed and recognized for nearly a century, to refer to the fact that waves moving along with the cyclone are further amplified (see for example Cline, 1920; Tannehill, 1936). King and Shemdin (1978) proposed the concept of "extended fetch" or "trapped fetch" in tropical cyclones. This idea has been further developed and applied to real cyclones in particular by Young (1988) and Bowyer and MacAfee (2005).

In the right quadrants of TCs, waves are indeed subject to high wind forcing conditions for longer periods than usual, because of the translation of the TC: because they move forward with the TC, they experience an extended fetch. The translation speed of the TC plays a critical role in such a wave containment. On the contrary, waves in the left quadrants propagate backward, opposite to the cyclone motion: in this quadrant, the motion of the TC

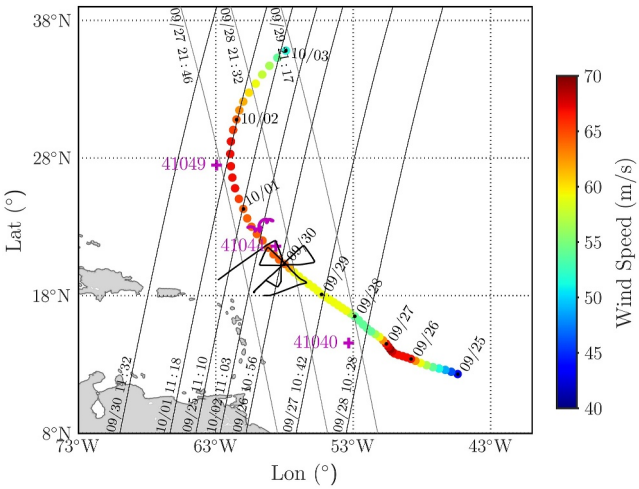

Figure 1. Trajectory of Hurricane Sam between 25 September 2021 and 3 October 2021. Colors: maximum sustained wind speed in $m{\cdot}s^{-1}$(IBTrACs data). Magenta crosses: location of the NDBC buoys 41040, 41044, and 41049. Magenta line north of buoy 41044: trajectory of the SD 1045 during the same period. Thick black line: reconnaissance flight path on the night of 29–30 September. Gray and black lines: ascending and descending nadir tracks of CFOSAT in the vicinity of the in situ devices during that period (the corresponding time is also indicated).

tends to reduce the fetch duration. A one-dimensional analytical model for wave field evolution forced by wind in the right and left quadrants of a moving TC has been proposed by Kudryavtsev et al. (2015). This analytical model (hereafter KGC15 model) is an extension of the self-similarity theory for wave growth (e.g., Badulin et al., 2007) to a moving frame of reference: that of the TC. In the KGC15 model, the wind blows along the direction parallel to the TC axis with a constant speed and generates waves propagating along the same direction. It has been recently extended to a numerical Lagrangian model of the evolution of wave properties along wave rays propagating in TC varying wind fields (Kudryavtsev et al., 2021a, 2021b). Understanding the wave distribution in TCs is still an open issue. In the present paper, the existence of trapped waves in Hurricane Sam will be investigated using observational data.

This paper is a multi-data sources investigation of Hurricane Sam, a category 4 major hurricane formed on 22 September 2021 and dissipated on 7 October 2021, with maximum sustained winds of 70 $m{\cdot}s^{-1}$. Our study is based on satellite, airborne and in situ measurements, including NDBC buoys and a saildrone which crossed Sam while it was in category 4. To the best of our knowledge, this is the first time the wave measurements in a TC by a saildrone are used in this context.

2. Data Sets and Methods

The parameters of tropical storms and hurricanes are available in the International Best Track Archive for Climate Stewardship (IBTrACS, version 4) database (Knapp et al., 2010). Best track data from the US agency, providing 3-hourly data including locations and maximum sustained wind speed, were used here.

Figure 1 shows the trajectory of Sam between 25 September and 3 October 2021. During most of this period, its maximum sustained winds were larger than 50 $m{\cdot}s^{-1}$ (category 3). It strengthened to category 4 (winds larger than 58 $m{\cdot}s^{-1}$) first between 25 September 18:00 and 27 September 06:00, and then between 28 September 06:00 and 2 October 12:00. The locations of the NDBC buoys and the trajectory of the SD 1045 between 25 September and 3 October are indicated in magenta in Figure 1. A few hours after its first intense phase, the track of Sam passed within 188 km east of the NDBC buoy 41040, whereas during its second intense phase, it passed within 60 km west of the NDBC buoy 41044, 30 km west of the saildrone 1045 and 103 km east of the buoy 41049.

The results presented in Section 3.3 also rely on SWIM and NDBC waves measurements in four tropical storms (Sebastien in 2019, Josephine in 2020, Claudette and Fred in 2021), one hurricane of Category 1 (Isaias in 2020), two hurricanes of Category 2 (Sally in 2020 and Earl in 2022) and one hurricane of Category 4 (Ida in 2021).

2.1. In Situ Observations

The NDBC buoys provide hourly one-dimensional frequency wave spectra typically from 0.03 to 0.40 Hz as well as 5 Fourier coefficients corresponding to the directional energy distribution. Two-directional frequency wave spectra are reconstructed using the Maximum Entropy Estimation (MEM) method (Lygre & Krogstad, 1986). Wave parameters, including the SWH, the dominant wave period and the corresponding direction of propagation, are also provided on an hourly basis. The SD data include only the SWH and the peak period of waves every 30 min. Unfortunately, no information about the spectral distribution or the direction of propagation of waves is provided by the SD. NDBC buoys (resp. SD) also provide wind measurements (speed and direction) every 10 min (resp. 30 minutes). These measurements are performed at the anemometer height. For a proper comparison with other wind measurements, the corresponding 10 m height winds were retrieved using the correction method proposed by Zieger et al. (2009), assuming a logarithmic marine boundary layer under neutral stability conditions. Note that the winds measured by the SD 1045 during Sam were earlier successfully compared to satellite microwave radiometer measurements and models by Ricciardulli et al. (2022).

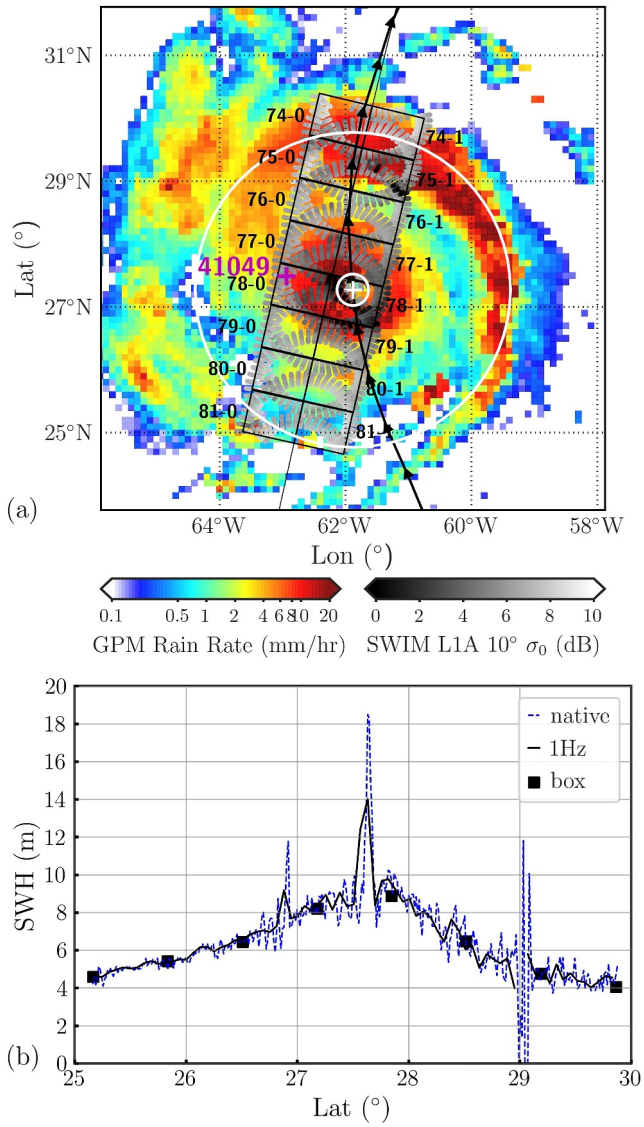

Figure 2. (a) SWIM footprints of the spectral beam at 10° during the passage of SWIM within Sam on 1st October 11:32. Gray shades: values of σ_0 (in dB) along the footprints. In black: boxes of the L2 wave products, each side of the nadir track. In colors: rain field (mm/hr) on 1st October 11:30. Thick black line: trajectory of the center of Sam. White cross: location of the center of Sam during the passage of SWIM. White circles: R_{max} and 10 R_{max}. Magenta cross: location of buoy 41049. (b) SWH as measured by SWIM along the nadir track: native (dashed blue), 1 Hz averaged (black) and averaged over the along-track size of each wave box (black squares).

2.2. Satellite and Airborne Wave Products

The in situ wave measurements were complemented by satellite wave products. CFOSAT has passed several times within Sam, as highlighted by Figure 1, on which the nadir tracks of CFOSAT in the vicinity of the in situ devices (at a distance less than 300 km) have been superimposed for the period 25 September–3 October. The passage of 1st October 11:32 is of particular interest because it was very close to the TC center (Figure 2a). The nadir beam of SWIM provides SWH measurements (Figure 2b) whereas the 3 off-nadir (or spectral) beams inclined at 6°, 8°, and 10° with respect to nadir provide two-dimensional wave slope spectra. In the present study, we use the wave spectra contained in the level 2 (L2) products provided by the CNES Wind and Wave Instrument Center (CWWIC). We mainly use the products derived from the spectral beam at 10°, which tends to be preferred by the community because it is less affected by speckle contamination and wind (Hauser et al., 2021).

The detailed investigation of the impact of rain on SWIM wave spectra carried out in Section 4 deserves some details on the geometry and post-processing chain of the SWIM instrument. First, the Normalized Radar Cross Section (NRCS) signals, hereafter denoted as σ_0, are computed within the footprint along the look direction (about 18 km long for the 3 dB footprint) with a high resolution (about 8 m when projected on the surface). Because SWIM is a real-aperture radar, these σ_0 values correspond to signals integrated over the azimuth direction (3 dB footprint of about 18 km). The gray segments shown in Figure 2a show an example of the sampling for successive azimuthal scans of the SWIM. Each gray segment represents the position of the footprint in the look direction (the azimuth extension is not represented here). In the post-processing, to avoid conditions of low signal-to-noise ratio, only the values larger than a threshold value are kept (3 dB above the thermal noise level). The σ_0 signals contain modulations due to the tilt of the long waves when these propagate along the look direction (Hauser et al., 2021). To retrieve the wave information from the σ_0 measurements, a detrending is applied on the σ_0 profiles, and the fluctuation signals, $\delta\sigma_0$, are then calculated. Modulation spectra, hereafter Pm(k), are then derived from $\delta\sigma_0$ through a Fourier transform, corrected from the speckle noise spectrum and the sensor impulse response spectrum. The modulation spectra are then transformed into wave slope spectra by applying a Modulation Transfer Function (MTF), which involves a renormalization (see below). The different directions are finally combined to construct a two-dimensional wave slope spectrum at the scale of a box (black rectangles in Figure 2a) of about 70 km × 90 km, on each side of the nadir track. As explained above, the spectral energy is normalized using the SWH from the nadir beam. More precisely, the native nadir SWH (dashed blue curve in Figure 2b) is averaged over each box, resulting in the values highlighted by the black squares in Figure 2b and used to normalize the wave spectra. In this averaging process, the values larger than 3 times the standard deviation of the series are deleted. The thus-obtained wave spectra are discretized in 32 wave numbers in the range [0.01–0.28] m^{-1} and 12 directions of propagation, with a 180° ambiguity (see Hauser et al., 2021, for further details). In addition to the L2 products, containing the wave spectra, Section 4 also relies on the L1A and L1B products provided by the CWWIC, which contain the σ_0, $\delta\sigma_0$ and Pm variables. An alternative post-processing, involving running averages along the footprints, is proposed by the Ifremer Wind and Wave Operation Center (IWWOC) to build the L2S SWIM products, containing one-dimensional wave slope spectra along the footprints. These data are also used in Section 4.

Sentinel 3 has passed twice over Sam: on 30 September 01:34 and on 1st October 01:49. The present study also involves the 1 Hz averaged L2P SWH and surface wind measurements by the Sar Radar ALtimeter (SRAL)

onboard Sentinel 3. Besides, Hurricane Sam was also sampled by the SAR of Sentinel 1. Among the passages of Sentinel 1, the passages on 2 October 09:54 and 3 October 09:45 are of particular interest, because they are very close (both in space and time) to SWIM. The level 2 products of the Sentinel 1a and 1b SAR wave mode were used. They correspond to two-dimensional wave height spectra, built from imagettes of size 20 km × 20 km, and discretized in 60 wavenumber bins in the range [0.01–0.21] m^{-1} and 72 directions from 0° to 360°.

Finally, during Hurricane Sam, 4 reconnaissance flights were performed by NOAA. The flight path on the night of 29–30 September, used later in this study, is represented in black in Figure 1. The airborne Wide Swath Radar Altimeter (WSRA), which is a radar altimeter operating at 16 GHz, provides real-time continuous wave measurements. We used the level 4 (L4) product which contains two-dimensional wave spectra $E(k_x, k_y)$ of 65 × 65 spectral values, where k_x and k_y are the east and north components of the wavenumber vector. They correspond to spectra whose 180° ambiguity has been removed by the method described in Popstefanija et al. (2021).

2.3. Wind and Rain Products

The wave distribution in TCs is partly correlated to the surface wind field. In addition to the wind measurements by the NDBC buoys and the SD, our study also relies on satellite wind measurements, as well as model outputs. We used the CSCAT L2B wind products of 25-km grid resolution provided by the National Satellite Ocean Application Service (NSOAS). It was recently shown by Zhao et al. (2022) that for high winds (above 15 m/s) and for rain rates up to 6 mm/hr, there is a good agreement between the CSCAT winds and the European Centre for Medium-Range Weather Forecasts (ECMWF) winds. However, it must be kept in mind that they also show that the CSCAT winds retrieved within Typhoon Maysak (2020) are underestimated (compared to ECMWF) for heavy rain conditions (rain rate larger than 6 mm/hr). These data are completed by the surface wind outputs of the ECMWF Integrated Forecasting System (IFS, version 47r1) on a 0.1° × 0.1° grid available every 6 hr. It is worth noting that, thanks to a new roughness length parameterization (considering the roughnesslength decrease under extreme wind conditions), the ECMWF IFS numerical simulations in version 47r1 perform much better than the previous versions in capturing the high winds in tropical cyclones (e.g., Bidlot et al., 2020; Li et al., 2021).

The rain rate (hereafter *RR*) is estimated using the Integrated Multi-satellitE Retrievals for GPM (IMERG) Final Run product. The IMERG product integrates all microwave precipitation estimates from GPM constellation and Infrared-based observations, with Global Precipitation Climatology Centre monthly gauge calibration, including a backward and forward morphing technique (Huffman et al., 2023). The IMERG product in version 7 is half-hourly computed on a 0.1° × 0.1° spatial grid. Only data with a quality index larger than 0.6 are considered in the present study.

2.4. Methods

The natural spectral variable for in situ observations being the frequency, the SWIM wave slope spectra $F(k, \theta)$ (in m^2) are converted to wave height spectra $E(k, \theta)$ (in m^4) and then to frequency wave spectra $\widetilde{E}(f,\theta)$ (in $m^2 \cdot s$) using the formula

$$E(k,\theta) = \frac{F(k,\theta)}{k^2}, \qquad \widetilde{E}(f,\theta) = E(k,\theta)k\frac{dk}{df}, \tag{1}$$

and the gravity waves dispersion relation. The SWH is estimated as

$$SWH = 4\sqrt{E_{tot}} \qquad \text{where} \qquad E_{tot} = \iint_0^{\pi} \widetilde{E}(f,\theta)\, df d\theta, \tag{2}$$

a double integration being performed over the directions θ and the frequencies f. The dominant frequency, f_p (resp. dominant wavelength λ_p), and the dominant direction, θ_p, provided in the NDBC (resp. SWIM) products have been estimated using different procedures, which prevent proper comparisons. These parameters are thus recalculated here using the frequency wave spectra $\widetilde{E}(f,\theta)$. Following Le Merle et al. (2022), a two-dimensional Gaussian filter is applied to the directional spectra to attenuate the spurious energy peaks that can form at low wavenumbers in the SWIM spectra, before applying the following formula

$$f_p = \frac{\int_{f_{max}-\Delta f}^{f_{max}+\Delta f} f\ \widetilde{E}(f,\theta_{max})\,df}{\int_{f_{max}-\Delta f}^{f_{max}+\Delta f} \widetilde{E}(f,\theta_{max})\,df}, \qquad \theta_p = \frac{\int_{\theta_{max}-\Delta\theta}^{\theta_{max}+\Delta\theta} \theta\ \widetilde{E}(f,\theta_{max})\,d\theta}{\int_{\theta_{max}-\Delta\theta}^{\theta_{max}+\Delta\theta} \widetilde{E}(f,\theta_{max})\,d\theta}, \tag{3}$$

where (f_{max}, θ_{max}) is the location of the maximum energy, and $(\Delta f, \Delta\theta)$ are the frequency and direction intervals. The same procedure was applied to the SAR and WSRA wave height spectra. The direction convention for θ is the direction from which waves travel, measured clockwise from North. The dominant wavelength λ_p is deduced from f_p using the dispersion relation.

The following study involves distance calculations between SWIM and in situ measurements. The fact that the SWH measurements are performed along the nadir track (black line in Figure 2), whereas the wave spectra (hence the λ_p and θ_p parameters) are computed over boxes (black quadrangles in Figure 2), is taken into account when calculating the distance between measurements.

3. Waves Observations by SWIM and In Situ Devices

In this section, the in situ observations by NDBC buoys and the SD 1045 are used and compared to the SWIM wave spectra. In addition, to assess the reliability of the SWIM wave spectra under heavy rain conditions, SWIM wave spectra are compared to NDBC wave spectra within 8 other tropical storms and hurricanes.

3.1. Multi-Sources Composite Description of Wind and Waves Conditions in Sam

A composite over 3.5 days is first built, using all of the available observations, in order to characterize the wave distribution in Hurricane Sam. Figure 3 is a composite constructed using different data sources over 3.5 days, between 29 September 00:00 and 2 October 12:00. That period corresponds to the second high-intensity phase of Sam. During that period, its maximum sustained winds were comprised between 59 $m{\cdot}s^{-1}$ and 67 $m{\cdot}s^{-1}$, which corresponds to a relative change in intensity of about 10%. However, the cyclone tends to accelerate during this period, with a propagation speed increasing from 4 to 8 m/s. The radius of maximum winds, R_{max}, is constant for most of that period. Indeed, based on IBTrACS data, R_{max} is 28 km from 29 September 00:00 until 1st October 12:00. The radius of maximum winds then increases and stabilizes at 37 km. The average value of R_{max} over this period, 30 km, is used in Figure 3. All measurements are reported in the frame of Sam, with the top of the figure corresponding to the TC propagation direction. Velocities correspond to flows in the Earth's frame. The figure presents both waves and winds in situ measurements by the 3 NDBC buoys (41040, 41044 and 41049) and by the saildrone SD 1045. The wave measurements by SWIM during 3 passages (on 29 September 22:32, 1st October 11:32 and 2 October 11:16) are superimposed, as well as the SWH measured by the Sentinel-3 altimeter during the two passages on 30 September 01:34 and 1st October 01:49. The WSRA wave data collected during the reconnaissance flight performed between 29 September 20:38 and 30 September 03:03 are also reported on the same figure. Finally, the CSCAT winds are also plotted in Figure 3d, at the position of the SWIM wave boxes. It is worth noting that in this type of representation, the information on the temporal evolution of the wave field is not easily read. To complement this figure, an animation in time is thus provided as Supporting Information S1.

Figures 3a–3c show the SWH, the dominant wavelength and the dominant wave directions, respectively, whereas Figure 3d shows the wind vectors. In Figure 3c, the 180° ambiguity inherent to the SWIM wave spectra is raised using the CSCAT winds, by assuming that under TCs conditions, the deviation of wave direction from the wind varies between 0° and 180° to the right, which has been observed in many previous studies (e.g., Young, 2017). The largest waves are observed near the TC center and in the right front quadrant at distances smaller than 3 R_{max} (Figure 3a), whereas the longest wavelengths are observed in the left front and right front quadrants (Figure 3b). Waves in the two front quadrants radiate out of a region to the right of the hurricane center, corresponding to a region of strong wind (see Figures 3d and 5b which shows the CSCAT wind field on 1st October 11:32). It is worth noting that wind and dominant waves are never aligned. The angle between winds and waves is about 60° in the right front quadrant, and larger than 60° in most locations in the other quadrants (compare Figures 3c and 3d).

It is interesting to compare these results to Le Merle et al. (2022). Between 29 September 00:00 and 2 October 12:00, the displacement velocity V of Sam increased from 3.6 to 9.3 $m{\cdot}s^{-1}$ on 1st October 18:00 before decreasing to 7.7 $m{\cdot}s^{-1}$. The ratio between the maximum sustained wind U_{max} and the displacement velocity V was mainly

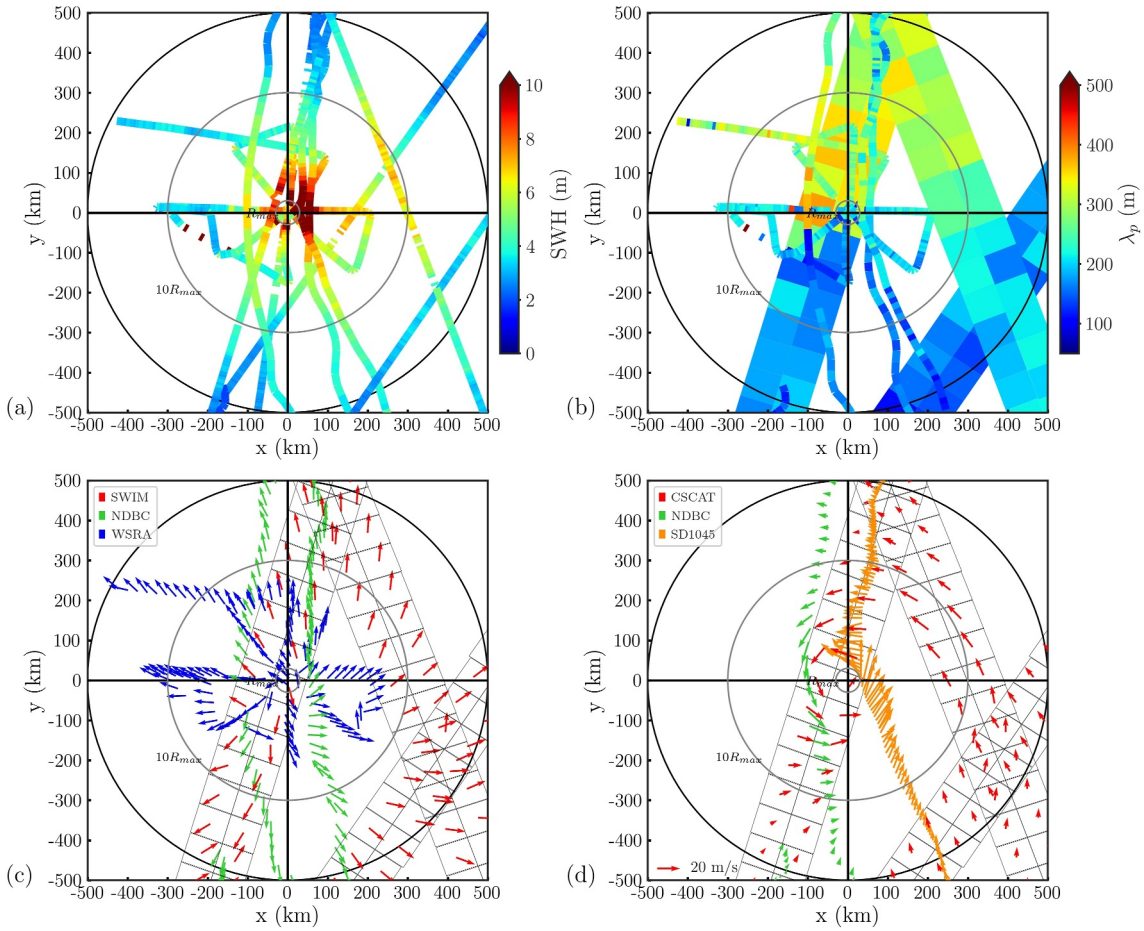

Figure 3. Composite representation of observations between 29 September 00:00 and 2 October 12:00 reported in the frame of Hurricane Sam. (a) SWH from SWIM, Sentinel 3, the airborne WSRA radar, 3 NDBC buoys and the SD, (b) Dominant wavelength λ_p from SWIM (large squares), the airborne WSRA radar, 3 NDBC buoys and the SD, (c) Dominant wave direction from SWIM, the airborne WSRA radar and 3 NDBC buoys (see inset for color code), (d) Wind vectors from CSCAT, 2 NDBC buoys and the SD (see inset for color code). Black circles indicate $R_{\max}$, 10 $R_{\max}$ and a radius of 500 km, with $R_{\max}$ = 30 km.

comprised between 5 and 12, which corresponds to a moderate speed TC, according to their classification. The above description is thus consistent with the results obtained by Le Merle et al. (2022) for moderate speed TCs.

3.2. SWIM and In Situ Estimations of Wave Parameters in Sam

In order to assess the reliability of SWIM wave measurements in Hurricane Sam, a comparison of the wave parameters as measured by SWIM and by the in situ devices is performed. Data provided by the NDBC buoys and by the SD are considered here as the most reliable wave measurements in Sam. The main issue raised when comparing satellite to in situ measurements is due to the sparse nature of these two types of data, both in space and time. On the one hand, the in situ observations are performed at the sole location of the device, which is fixed for the NDBC buoys and which changes over time for the SD, according to its trajectory. These data are provided every 10 min for the NDBC buoys (hourly for the spectra) and every 30 min for the SD. On the other hand, SWIM passages in a given region of the globe take place once or twice a day, and the wave measurements are performed only along the nadir track (for the SWH) and in two bands of about 90 km wide on each side of the track (for the wave spectra). There is therefore inevitably a temporal and spatial difference between the SWIM and in situ measurements. Such differences can be critical under TCs because of the inhomogeneous distribution of waves in TCs and because of their temporal variability, due to the wind temporal variations and to the TC displacement. Such comparisons must thus be performed carefully, especially when assessing the quality of satellite measurements.

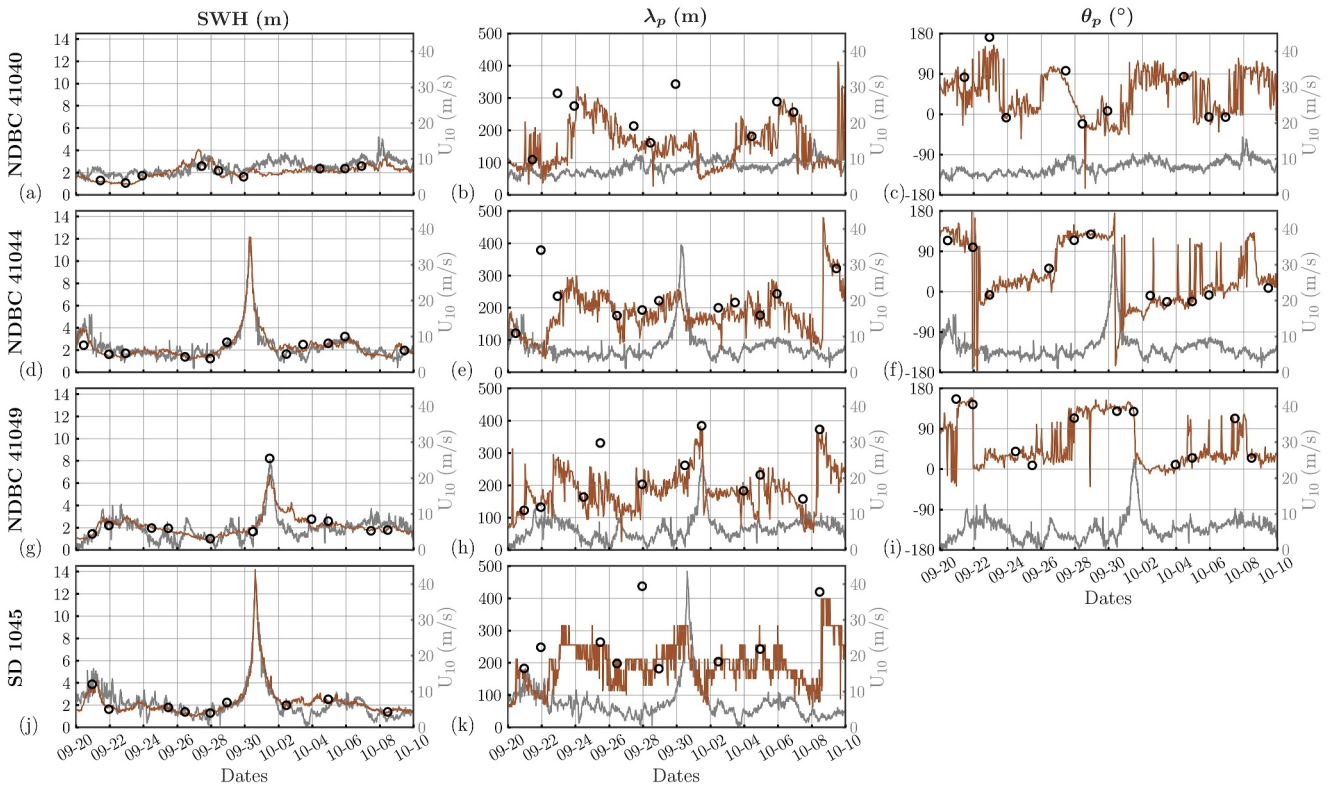

Figure 4. Brown curves: SWH (first column), dominant wavelength λ_p (second column) and dominant direction θ_p (third column) measured by the buoys 41040 (first row), 41044 (second row), 41049 (third row) and the SD 1045 (fourth row). Gray curves: wind speed (corresponding scale on the right of the panels). The abscissa corresponds to time, between 20 September and 10 October. Black circles: closest SWIM measurements.

The brown lines in Figure 4 show the time evolution of the SWH (first column), the dominant wavelength λ_p (second column) and the dominant direction θ_p (third column), measured by the buoys 41040 (first row), 41044 (second row), 41049 (third row) and the SD 1045 (fourth row) between 20 September and 10 October. The parameters λ_p and θ_p are calculated using the method described in Section 2.4. The directional convention for θ_p is "coming from", measured clockwise from North (i.e., 90° indicates coming from East). Note that the saildrone data do not contain information on wave propagation direction. The gray curves correspond to the wind speed measured by the buoys and the SD.

For each device, we searched for co-localized measurements from SWIM, by allowing a maximum distance of 300 km between the SWIM box and the in situ device, and a maximum time-lapse of 30 min for the buoys and of 15 min for the SD. We further checked that the collocated SWIM and in situ data were located in the same quadrant of Sam. Figure 1 shows a sample of the nadir tracks corresponding to SWIM data used for collocation (they correspond to the period between 25 September and 3 October). For each device, we identified about 10 collocated SWIM measurements between 20 September and 10 October, which makes a total of 40 collocation pairs; these data correspond to different locations and different times. The wave parameters derived from the 40 collocated SWIM wave spectra are superimposed as black circles in Figure 4. In Figures 4c, 4f, and 4i, the 180° ambiguity on SWIM spectra was raised by selecting the direction closest to that measured by the buoy.

Buoys 41040 and 41049 provide measurements in the left quadrants of Sam (see Figure 1). Buoy 41040 is the furthest one from the TC track: it measured a maximum SWH of 4.1 m on 27 September 06:40 (panel a), while it was located about 250 km ahead of Sam (see Figure 1). Buoy 41049 measured a maximum SWH of 6.7 m on 1st October 11:40 (panel g), at about 100 km from the TC center. The buoy 41044 and the SD offer, on the other hand, measurements in the right quadrants (see Figure 1). Buoy 41044 measured a maximum SWH of 12.2 m on 30 September 08:40 (panel d), at about 60 km from the TC center, whereas the SD measured a maximum SWH of 14.2 m on 30 September 15:00 (panel j), while it was located only 35 km away from the TC center. There is an almost simultaneous occurrence between the maximum of SWH and the maximum wind speed as measured by

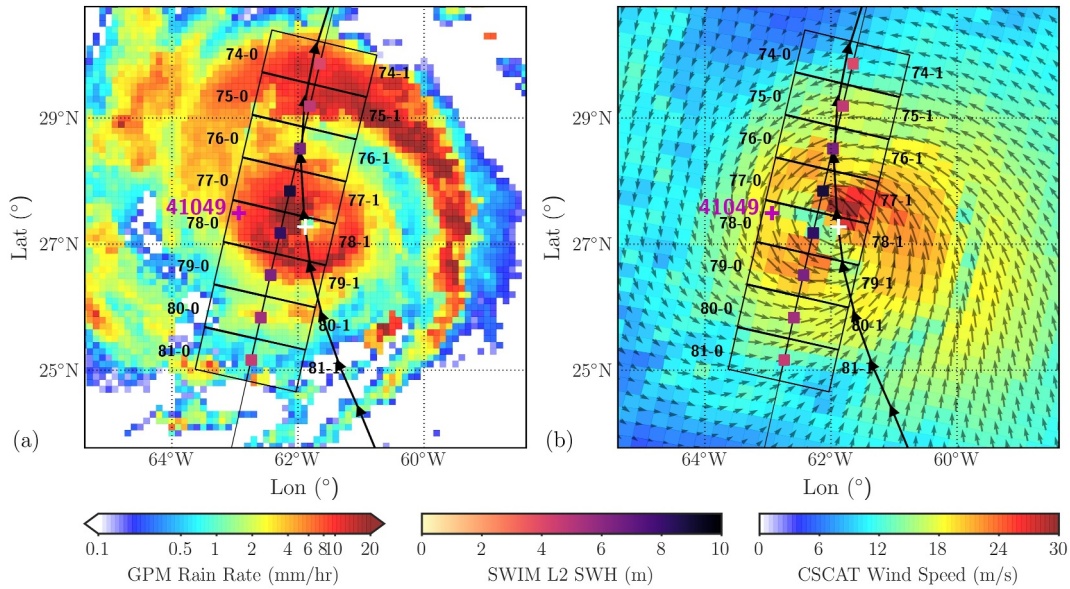

Figure 5. SWIM nadir track (black line) and boxes (black quadrangles) during the passage of SWIM within Sam on 1st October 11:32, close to the buoy 41049 (magenta cross). (a) Rain rate field (in mm/hr) on 1st October 11:30 and (b) surface wind field from CSCAT (colors: intensity in m/s, arrows: directions). Colored squares: nadir SWH averaged over boxes. Thick black line: trajectory of the center of Sam. White cross: location of the center of Sam during the passage of SWIM.

the buoys 41044, 41049 and by the SD, with maximum wind speeds of 24.4, 34.6, and 43.5 $m{\cdot}s^{-1}$ resp. (compare the brown and gray curves in panels d, g and j). By chance, we identified a SWIM measurement collocated with the buoy 41049 on 1st October 11:32, within Sam; SWIM measured a SWH of 8.2 m (panel g). Unfortunately, there was no passage of SWIM in the vinicity of the buoy 41044 and of the SD between 28 September 22:46 and 2 October 11:18: both SWH peaks on panels d and j are thus not sampled by SWIM.

During the passage of SWIM close to the buoys 41044, 41049 and to the SD, the dominant wavelength undergoes a sharp decrease from larger values to smaller values concomitant with the maximum of wind and SWH. On 30 September, within a few hours, it decreases from 250 to 150 m for the buoy 41044 (panel e) and from 300 to 100 m for the SD (panel k). The same is observed for the buoy 41049 on 1st October, with a decrease of λ_p from 400 to 100 m (panel h). This result is consistent with Figure 3b: the in situ devices, first undergo the longest waves, in the front quadrants of Sam, before undergoing shorter waves in the rear quadrants. The direction of propagation of waves also undergoes an abrupt change during the passage of Sam synchronised with the maximum wind and SWH (panels f and i). Buoys 41044 and 41049 first measure waves propagating forward and then waves propagating backward. More precisely, the direction from which waves are coming from shifts from South-East to North-West in the case of buoy 41044 (panel f), whereas it shifts from South-East to North for buoy 41049 (panel i). This corresponds to the change of direction between the front and rear quadrants also evidenced in Figure 3c with the green arrows.

The comparison of wave characteristics between SWIM measurements and in situ observations over the whole period shown in Figure 4 exhibits overall consistency. The discrepancy between the SWIM and in situ SWH is of order of 10% and does not exceed 30%. There are a few cases where the peak values, particularly the λ_p values, differ significantly. These discrepancies do not appear to be correlated to the spatial distance between the measurements. These cases correspond either to multi-modal systems with different wavelengths and directions but comparable energies, or to low SWH cases, where it is known that, despite filtering, SWIM spectra are biased by spurious peaks at low wavenumber (e.g., Hauser et al., 2021; Xu et al., 2022).

3.3. Two-Dimensional Wave Spectra in Heavy Rain

During the entire period subject to investigation here, the passage of SWIM within Sam on 1st October 11:32, very close to the buoy 41049, corresponds to heavy rain along the SWIM track. In the following, we will focus on this track. Figure 5 shows the nadir track and boxes over which the wave spectra are computed, superimposed to

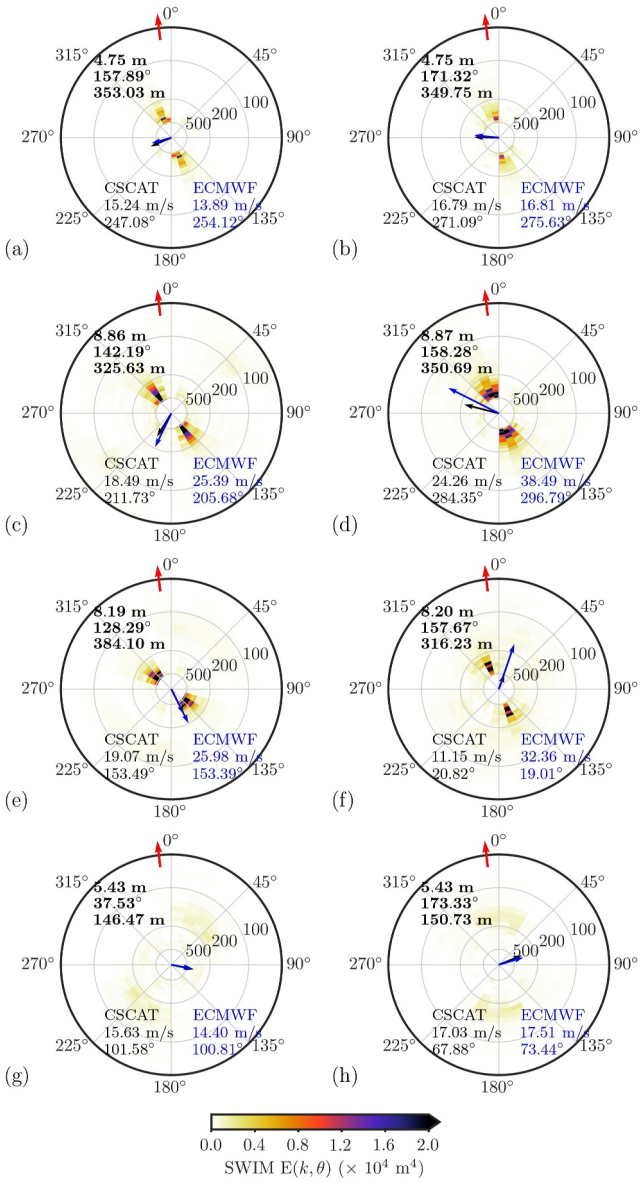

Figure 6. Two-dimensional wave height spectra E(k, θ) measured by SWIM in boxes (a) 75-0, (b) 75-1, (c) 77-0, (d) 77-1, (e) 78-0, (f) 78-1, (g) 80-0 and (f) 80-1. Black arrows: local wind vectors from CSCAT, blue arrow: ECMWF wind vector (wind speed and direction are indicated in the lower part of the spectra). Red arrows on the outer circle of the spectra: propagation direction of Sam. The parameters SWH, θ_p and λ_p as estimated from SWIM are indicated in the top-left part of the spectra.

the rain rate field at 11:30 (Figure 5a) and to the wind field measured by CSCAT (Figure 5b). Boxes numbered as 77-0, 77-1, 78-0, and 78-1 are the most severely affected by rain, with the rain rate exceeding 20 mm/hr in some areas of these boxes (Figure 5a). The wind speed from CSCAT does not exceed 30 m·s^{-1}, which is largely underestimated, roughly by a factor of 2 compared to the IBTrACS estimation. Note that such saturation is not specific to CSCAT: it is known that at high wind speeds (winds larger than 30 m·s^{-1}), wind information from scatterometers saturates.

The SWIM nadir track is oriented at an angle of a few degrees to the right of the propagation direction of Sam and provides spectra close to its propagation axis. A sample of the spectra located within 10 R_{max} of the center is shown in Figure 6. The highest SWH is measured by the two spectra 77-0 and 77-1, at the front of the center (Figures 6c and 6d). All spectra shown in Figure 6 exhibit dominant waves corresponding to remotely generated swell, with the largest wavelengths at the front of Sam (Figures 6a and 6b) as well as near the center (Figures 6c–6f). In the left rear quadrant, we observe shorter wavelengths (about 150 m) with a significant directional spreading of the energy (Figures 6g and 6h). The four spectra 77-0, 77-1, 78-0 and 78-1 shown in Figures 6–6f provide informations very close to the center of Sam, the corresponding boxes being located within 5 R_{max} from the center, whereas box 78-1 (Figure 6f) lies within 2 R_{max}. These four spectra are quite similar in terms of dominant wavelength. Spectra 77-0 and 78-0, in the left-front quadrant, are consistent with waves propagating forward, to the left of the propagation direction of Sam (Figures 6c and 6e), whereas spectrum 77-1, at the front of the center, exhibits wave energy propagating forward in a direction closer to that of Sam's displacement (Figure 6d). Wave propagation considerations in the case of spectrum 78-1 (Figure 6e) are more difficult to interpret since the box, which has dimensions of 70 km by 90 km, covers the eye region, in which conditions are highly heterogeneous. The above description is consistent with previous studies of wave field in tropical cyclones, which, in some sense, suggests that SWIM wave spectra remain reliable despite heavy rain conditions.

To assess the reliability of SWIM wave spectra under heavy rain conditions, the wave height spectrum of box 78-0 is compared to that of buoy 41049, with the distance between the center of the box and the buoy being 33 km and the time-lapse being only 8 min. These are the closest SWIM and in situ measurements available within TC Sam. The corresponding wave height spectra are shown in Figure 7. Both two-dimensional spectra shown in Figures 7a and 7b exhibit a dominant wave system characterized by a similar dominant wavelength (384 m for SWIM and 370 m for the buoy) coming from the south-east, with $\theta_p \approx 129°$ (with a 180° ambiguity for SWIM). However, the SWIM SWH (8.2 m) is overestimated by about 20% compared to the buoy SWH. Either the rain or the fact that the box is closer to the center of the cyclone by about 30 km compared to the buoy could explain this discrepancy. The omni-directional spectra $E_k(k)$ (in m^3), constructed as

$$E_k = \int_\theta E(k,\theta)\, k\, d\theta, \tag{4}$$

are shown in Figure 7c. Both profiles are comparable although the energy measured by SWIM at wavelengths larger than 100 m is larger than that measured by the buoy. A secondary wave system coming from the northeast is detected by both instruments, at a wavelength of 125 m according to SWIM and 100 m according to the NDBC buoy.

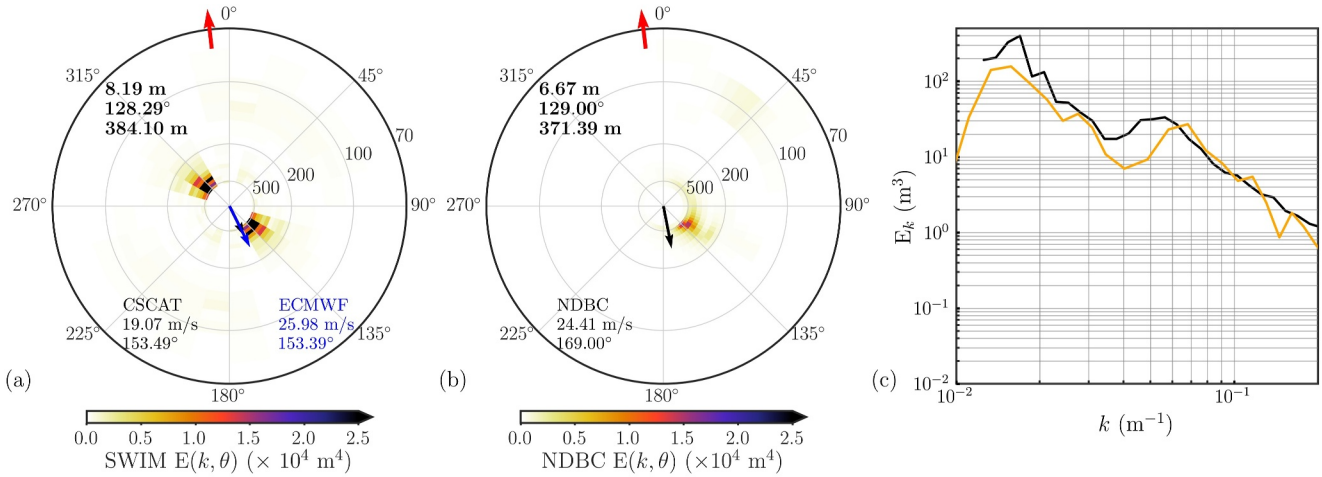

Figure 7. Two-dimensional wave height spectra E(k, θ) measured (a) by SWIM in box 78-0 (10° beam) on 1st October 11:32 and (b) by the NDBC buoy 41049 on 1st October 11:40. Black arrows: local wind vectors from (a) CSCAT and (b) from the buoy 41049, blue arrow: ECMWF wind vector in box 78-0 (wind speed and direction are indicated in the lower part of the spectra). Red arrows on the outer circle of the spectra: propagation direction of Sam. The parameters SWH, θ_p and λ_p are indicated in the top-left part of the spectra. (c): Corresponding SWIM (black) and NDBC (orange color) omni-directional wave spectra $E_k(k)$.

In the case of Sam, there are unfortunately no other such close comparisons of satellite and in situ measurements under high rainfall rates. In addition to Sam, we however also identified 8 tropical storms and hurricanes from 2019 to 2022 for which collocated SWIM and NDBC wave spectra close to the storm center are available, allowing a maximal distance between the box center and the buoy of 70 km. The 2D and 1D wave height spectra are shown in Figures 8 and 9 (they are ranked from largest to lowest SWH measured by SWIM). The maximum rain rate in the SWIM boxes varie from 0.2 to 48.5 mm/hr.

Even in the strongest rain cases (first and second row in Figure 8, second row in Figure 9), there is a good consistency between SWIM and in situ wave spectra, with the wave parameters differing by less than 20%. The SWIM and in situ 1D spectra are similar in the peak energy region and for larger values of wavenumber. However, they differ significantly at wave numbers lower than k_p. Indeed, SWIM is known to overestimate energy at small wave numbers, especially for SWH less than about 3 m (e.g., Jiang et al., 2022). This effect is clearly visible in the last two spectra shown in Figure 8 and in the four spectra in Figure 9. In the first case of Figure 8 (SWH larger than 6 m), we expect this effect to be less pronounced. A similar analysis to that conducted in Section 4 was carried out: the energy measured by SWIM at low wavenumbers does not appear to be related to rainfall. This case actually corresponds to measurements very close to the center of the cyclone (see Figure 8a) where spatial variability is significant, which could explain the discrepancy between the SWIM and in situ spectra at low wavenumbers. Another possible explanation could be an underestimation of buoy energy at the lowest frequencies, as can be observed in several publications that show comparisons of omni-directional wave spectra obtained from NDBC buoy and from SAR observations (see Lehner et al., 2012; Sun et al., 2024) or from optical observations (e.g., Hwang et al., 2000; Kudryavtsev et al., 2017). This is possibly due to a high-pass filter in the construction of directional wave spectra from measurements (see Earle, 2003).

The results shown in this section exhibit overall consistency between the SWIM and in situ measurements of wave parameters and wave spectra in the wave energy containing part (although some artifacts seem to appear at wavenumbers much lower than the peak of the spectra), even in the presence of heavy rain. Note that the SAR wave spectra acquired in cyclones are more challenging to use. Indeed, these spectra are impacted by the azimuth cut-off effect, which prevents measurements of the wind sea waves or short swell. The cut-off is particularly important for wave energy propagating in directions close to the SAR azimuth direction. This is highlighted in Appendix A where co-located SWIM and SAR spectra measured within Hurricane Sam are compared (see Figure A1 in Appendix A). Finally, we identified some cases in moderate to heavy rain conditions, where the SAR spectra exhibit a strong attenuation compared to SWIM, which can not be attributed to the cut-off effect (because corresponding to waves propagating in a direction closer to the range than to the azimuth direction) and which suggest that the spectra resulting from the 2D SAR imagettes are more strongly affected by rain than the 1D SWIM footprints (see Figure A2 in Appendix A).

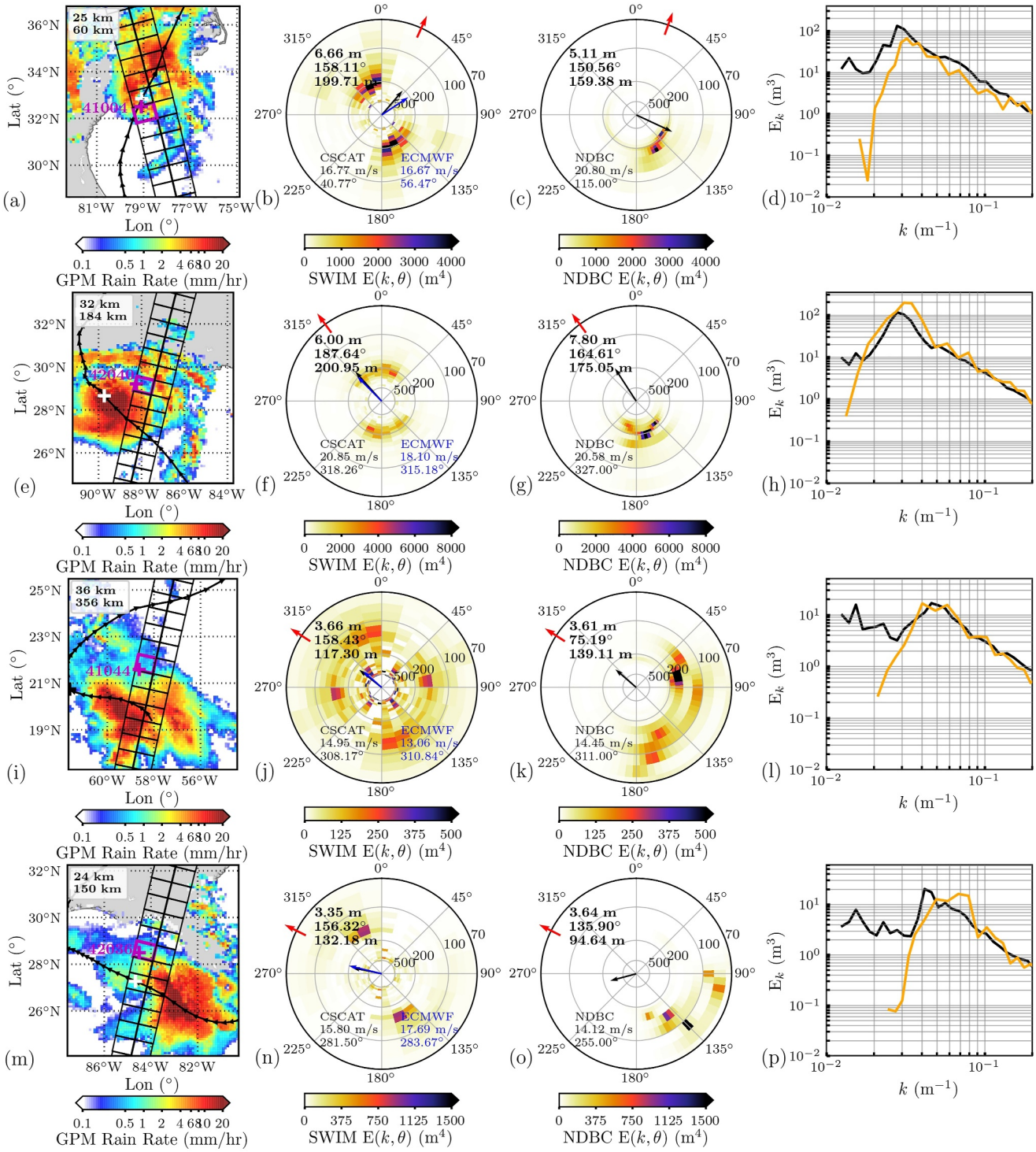

Figure 8. Comparison of directional and omni-directional wave spectra between SWIM and buoy measurements in hurricanes Isaias (first row, (b): 2020/08/04 00:06, (c): 2020/08/03 23:40), Ida (second row, (f): 2021/08/29 13:15, (g): 2021/08/29 13:40), tropical storm Sebastien (third row, (j): 2019/11/20 11:14, (k): 2019/11/20 11:40), and hurricane Sally (fourth row, (n): 2020/09/13 13:03, (o): 2020/09/13 12:40). First column: SWIM boxes (black quadrangles) superimposed to the rain rate field in mm/hr (in colors); thick black line: the best track of the storm; white cross: storm center during the passage of SWIM; magenta cross: NDBC buoy; white box: SWIM-buoy distance and SWIM-TC distance. Second column: SWIM wave height spectrum (closest box to the NDBC buoy, highlighted in magenta in the first column). Third column: NDBC wave height spectrum. Fourth column: 1D wave height spectra.

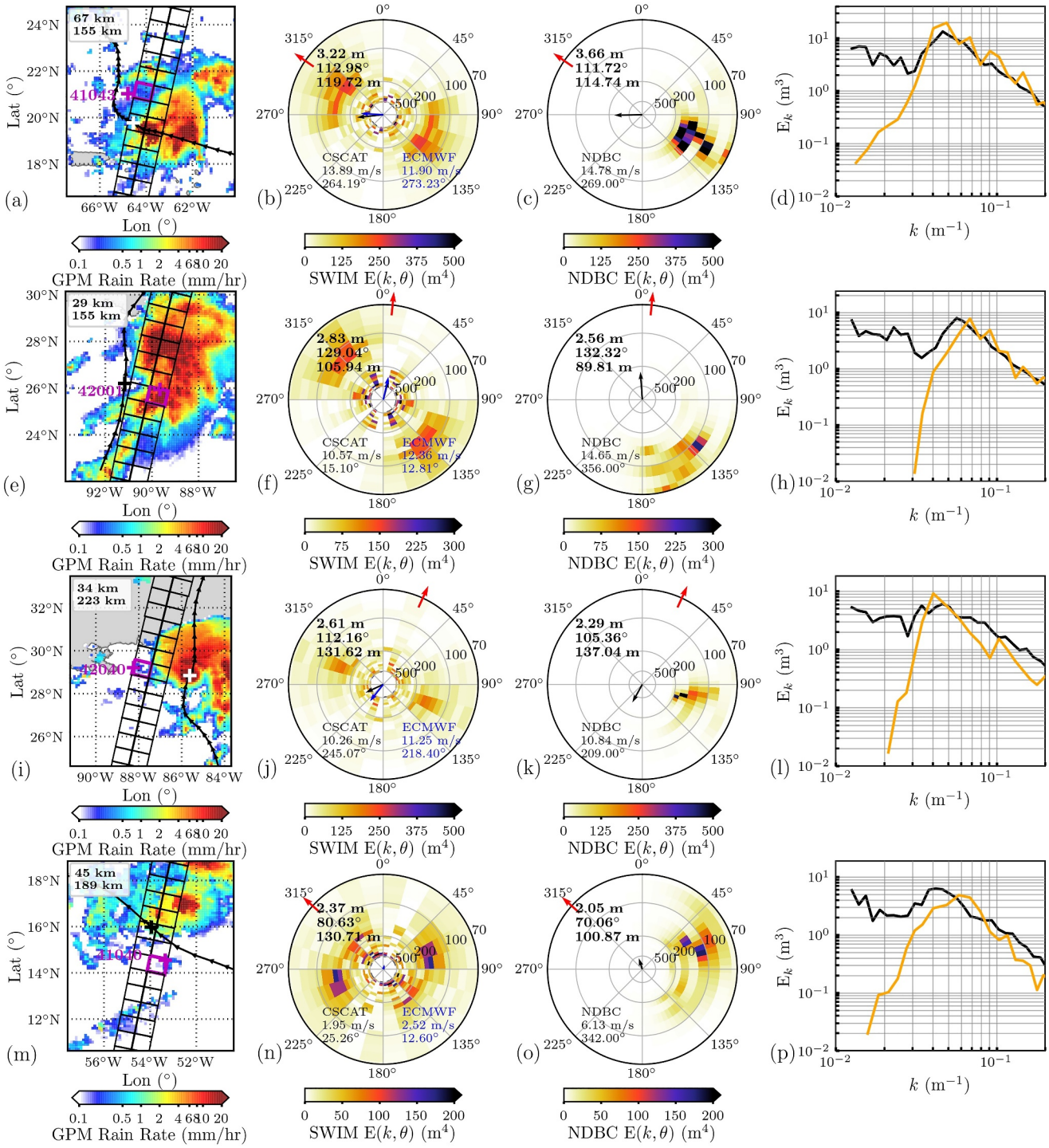

Figure 9. Same as Figure 8, for hurricane Earl (first row, (b): 2022/09/04 11:26, (c): 2022/09/04 11:40) and tropical storms Claudette (second row, (f): 2021/06/18 13:24, (g): 2021/06/18 13:40), Fred (third row, (j): 2021/08/16 13:15, (k): 2021/08/16 13:40) and Josephine (fourth row, (n): 2020/08/14 10:55, (o): 2020/08/14 10:40).

4. Rain Impact on SWIM Wave Spectra

The aim of this section is to understand why the SWIM wave spectra provide reliable information, even in heavy rain conditions. To do so, we focus on the passage of 1st October 2021 11:32 during hurricane Sam. The footprints corresponding to the spectral beam at 10° within 350 km from the TC center are shown in Figure 2a.

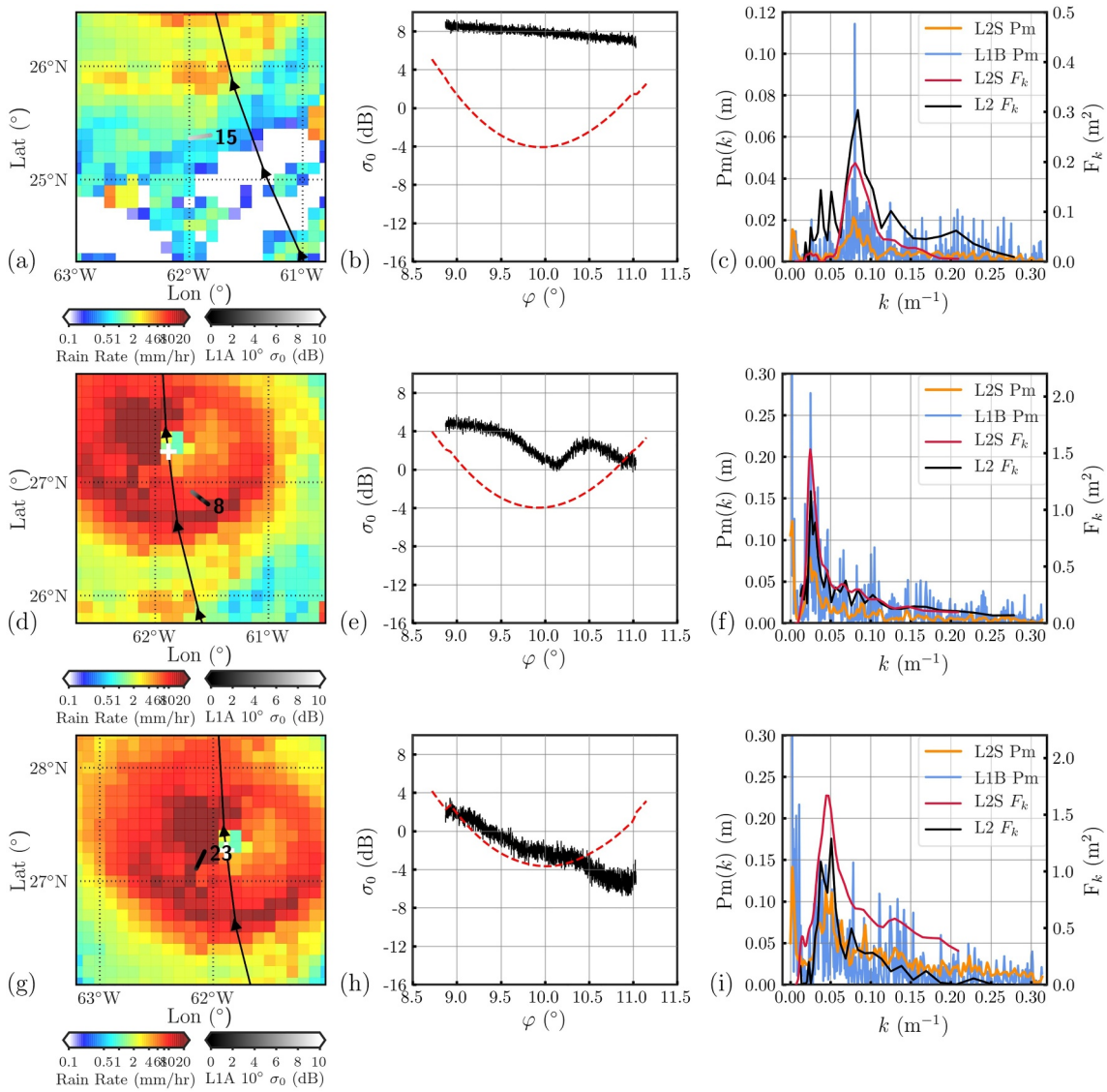

Figure 10. First column: rain rate field (colors) superimposed to the footprint (segment next to the footprint number). Gray scale: σ_0 values along the footprint. Second column: σ_0 profile (black) and noise equivalent σ_0 augmented by 3 dB (dashed red) as a function of incidence angle φ in the look direction. The intersection between the black and red curves delimits the incidence range used for the wave analysis. Third column: modulation spectra (vertical scale on the left-hand side axis) from L1B (blue line) and L2S (orange line) products, superimposed to wave slope spectra (vertical scale on the right-hand side axis) from L2 (black line) and L2S (red line) products. First row: case of light rain, 1.1 mm/hr (box 80-1, swath 15, $lsvar = 0.0284$, $\phi = 80°$, where ϕ denotes the azimuth direction). Second row: case of moderate rain, 9.4 mm/hr (box 78-1, swath 8, $lsvar = 0.784$, $\phi = 131°$). Third row: case of heavy rain, 24.6 mm/hr (box 78-1, swath 23, $lsvar = 0.364$, $\phi = 23°$).

4.1. Rain Impact on SWIM Radar Signals

We first focus on three footprints, one in light rain (1.1 mm/hr), the other one in moderate rain (9.4 mm/hr) and the third one in heavy rain (24.6 mm/hr). They are denoted as cases 1, 2 and 3 respectively. They correspond respectively to the first, second and third rows of Figure 10. The location of the footprint in the rain rate field is shown as a gray segment with a number close to it in the first column of Figure 10, whereas the σ_0 profile as a function of the incidence angle in the look direction is shown in the second column of Figure 10. The signal is attenuated by rain in cases 2 and 3, with the attenuation reaching 12 dB at the incidence of 11° in Case 3 compared to Case 1. Note that the parts of the signal which are too attenuated are filtered in the post-processing. The threshold fixed for this filtering corresponds to the noise equivalent σ_0 augmented by 3 dB (red dashed line in Figure 10). Whereas the signal-to-noise ratio is high in Case 1, at the far range of the footprint, the signal is close to noise in Case 2 and below noise in Case 3. As long as a significant part of the signal is larger than the threshold,

the post-treatment can be conducted. For example, in Case 3, the signal used as input to the wave analysis will be limited to the 9–10.5° range in incidence, whereas in Case 1, all values in the range 9–11° will be kept in the analysis. In Case 2, the far range will be limited to about 10.8°.

Additionally, rain inhomogeneities within the footprints can cause distortion of σ_0. This is particularly visible in Case 2 (Figure 10e) where σ_0 exhibits large-scale oscillations at a scale of the order of the swath length (about 20 km for beam 10°), much larger than 500 m. The standard deviation of the σ_0 profile around its mean value, after filtering by a low pass filter (filtering of length scales under 500 m, associated to waves) allows to quantify the large-scale variability within the footprint. Its value, denoted as *lsvar*, is indicated in the caption of Figure 10: rain inhomogeneities within the footprints, causing large-scale oscillations of the σ_0 profile, result in larger values of *lsvar*.

The modulation spectra derived through the Fourier transform of the detrended σ_0 signal, Pm(k), contained in the L1B (resp. L2S) products are shown in the third column of Figure 10 in blue (resp. orange) color lines. The large-scale oscillations of σ_0 in cases 2 and 3 yield a peak of energy in the modulation spectra at small k in Figures 10f and 10i. It is worth noting that the peak at small k is smaller in the L2S modulation spectra than in the L1B modulation spectra. Indeed, the L2S modulation spectra result from the Welch method (Welch, 1967) where the σ_0 values are split in 15 overlapping windows before being used as input of 15 fast Fourier transforms (FFT) whose spectral energy is then averaged to build the modulation spectrum. Such a process logically reduces the impact of the inhomogeneity of rain along the footprint. In contrast, in the L1B processing, the full length of the σ_0 samples is used as input to the FFT, which leads to more noisy modulation spectra, while the averaging is carried out in the spectral space during the construction of the two-dimensional wave slope spectrum, after filtering the low wavenumber components ($k < k_{\min} = 0.01$ m^{-1}). Hence, the comparison of L1B and L2S modulation spectra corroborates the correlation between the large-scale oscillations of σ_0 (as well as the resulting peak in the modulation spectrum at small k) and rain inhomogeneities along the footprint.

The above conclusions have been statistically verified using all the footprints within 350 km from the TC center during the passage of SWIM on 1st October 2021 (see Appendix B). In Appendix B, using SWIM 10° and 8° beams, we also show that rain mainly impacts the L1B modulation spectra at small wavenumbers (wavelengths larger than 1 km), rather than the waves range ([70–500] m). A similar study was conducted for the rainiest cases shown in Figures 8 and 9, leading to the same conclusions.

4.2. Rain Impact on L2 SWIM Wave Slope Spectra

The L2 (resp. L2S) wave slope spectra corresponding to the L1B (resp. L2S) modulation spectra are superimposed on the panels in the third column of Figure 10, in black (resp. red) color lines. They also exhibit a peak of energy corresponding to the waves propagating in the azimuth direction. However, in cases 2 and 3, they do not exhibit any peak at small wavenumbers, contrary to the modulation spectra. In the post-processing, values corresponding to wavenumbers smaller than $k_{\min} = 0.01$ m^{-1} are indeed filtered. Hence, the peak in the modulation spectra at small k due to the large-scale oscillations of σ_0 does not affect the wave slope spectra.

As explained in Section 2, the L2 two-dimensional wave slope spectra at the scale of a box are reconstructed by combining the measurements within the footprints contained in the box. Figure 11 gathers the parameters of the 25 footprints of the 10° beam in box 78-1 (see Figure B3a). The averaged $\overline{\sigma_0}$ over each footprint is most attenuated around the 30° and 190° directions, which are characterized by the highest rain rates; this results in large values of the *lsvar* parameter in these directions. The energy of waves in the modulation spectrum is quantified by $\mathcal{E}_{k>k_c}$ (defined in Appendix B), with $k_c = 2\pi \cdot 10^{-3}$ m^{-1}: it indicates that the dominant direction of waves lies around 150°. The dominant waves are thus detected by footprints undergoing moderate rain. Generally speaking, it is worth noting that because of the different locations of the footprints in the rain field, different situations are possible. In the configuration where the dominant waves direction coincides with footprints undergoing light or no rain (i.e., the footprints in stronger rain correspond to directions of low energy wave), the rain is not expected to affect the wave spectra, since the wave energy is measured by footprints in light or no rain. In other configurations, where the footprints measuring wave energy undergo moderate or heavy rain (like in Figure 11), we have shown in this section that as long as the attenuation is not too important, the wave spectra remain reliable.

It is important to note that the post-processing leading to the L2 wave slope spectra involves a normalization by the nadir SWH, retrieved from the shape of the waveform of the returned signal. A detailed study of the impact of

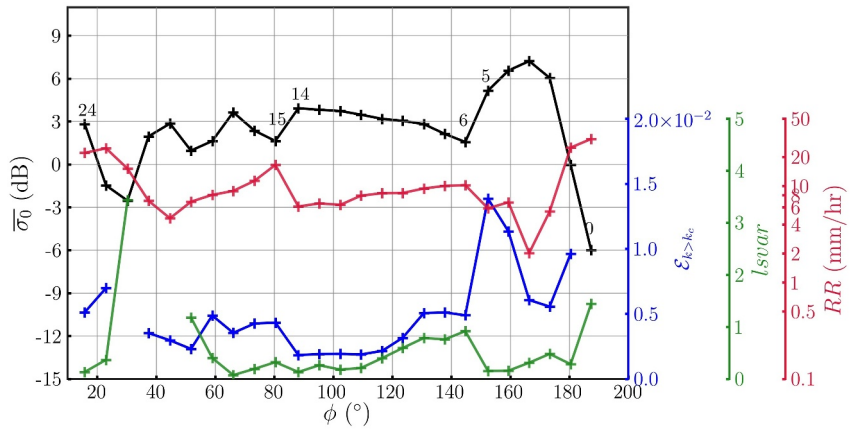

Figure 11. Values of $\overline{\sigma_0}$ (black), *RR* (red), *lsvar* parameter (green) and $\mathcal{E}_{k>k_c}$ (blue) as a function of the azimuth direction, corresponding to the 25 footprints of the 10° beam in box 78-1 (see Figure B3).

rain on SWH provided by the nadir measurements is out of the scope of the present paper. However, it can be noted that the comparisons presented in Figures 8 and 9 do not reveal a clear trend regarding the effect of rain on the nadir SWH.

5. Wave Asymmetry in Hurricane Sam

The largest waves for Sam are found in the right front quadrant, as highlighted in Figure 3a. The asymmetry in the wave field may simply originate from the asymmetry in the wind field (highlighted in Figures 3d and 5b), or may be due to the so-called extended fetch effect (Young, 1988). The aim of this section is to take advantage of the multiple measurements available in Hurricane Sam to investigate the physical origin of the wave asymmetry.

5.1. Analytical Model for Extended Fetch

The "extended fetch" idea has been recently formalized under simplifying assumptions by Kudryavtsev et al. (2015) here referred to as the KGC15 model.

The KGC15 model aims at predicting the waves properties of the strongest waves at a given location in the right and left quadrants of a TC, comprised between the $y = ax$ and $y = -ax$ reference lines. Kudryavtsev et al. (2015) used $a = 1$, which corresponds to a 45° angle; a slightly larger value, $a = 1.37$, is chosen here (corresponding to a 54° angle), in order to extend slightly the range of applicability of the model and thus allow comparison with more observational data.

In each quadrant, the wind speed u_w is supposed to be parallel to the TC axis and uniform along this direction and waves are assumed to propagate along the same direction. In a stationary TC, the oldest waves at a given position are those that originate from the line $y = -ax$, that is, at the rear of the right quadrant and at the front of the left quadrant. The former propagate toward the front and the latter toward the rear of the cyclone. The inverse wave age α_0 (defined as u_w/C_p, where C_p is the phase velocity of the wave) and the dimensionless energy $\widetilde{\mathrm{E}}_0$ (using u_w^4/g^2 as unit of energy) of the strongest waves at a given location in a stationary cyclone then take the form

$$\alpha_0 = c_\alpha \widetilde{\mathrm{Y}}^q \qquad \text{and} \qquad \widetilde{\mathrm{E}}_0 = c_e \widetilde{\mathrm{Y}}^p, \tag{5}$$

where $\widetilde{\mathrm{Y}}$ is the dimensionless fetch length (using u_w^2/g as unit of length). $\widetilde{\mathrm{Y}}$ is measured as the distance from the $y = -ax$ reference line ($\widetilde{\mathrm{Y}}$ is defined as a positive quantity in both quadrants). Following Kudryavtsev et al. (2015), the fetch law exponents p and q are chosen as $p = 0.89$ and $q = -0.275$, which yields $c_\alpha = 15.14$ and $c_e = 4.41 \times 10^{-7}$.

For a given position, knowing the corresponding wind u_w and distance $\widetilde{\mathrm{Y}}$, (5) provides the age and energy of the strongest waves. According to (5), a symmetrical wind field yields a symmetrical wave field. In the case of TC

moving at a constant velocity V, this symmetry is broken. The waves generated in the right quadrant first travel backward in the frame of the TC, their group velocity C_g being smaller than V. The dimensionless distance to be covered under the cyclone, for C_g to reach V, corresponds to the dimensionless critical fetch $\widetilde{\mathrm{L}}_{cr}$ defined as

$$\widetilde{\mathrm{L}}_{cr} = -c_\alpha^{-1/q}\frac{q}{1+q}\alpha_T^{1/q}, \tag{6}$$

$\alpha_T = u_w/(2V)$ being the inverse wave age when their group velocity equals the TC propagation speed V.

We note $\tilde{\ell}$ the dimensionless length of the segment between the $y = ax$ and $y = -ax$ lines (physical length normalized by u_w^2/g). There are then two possible scenarios depending on the value of $\tilde{\ell}$ compared to that of $\widetilde{\mathrm{L}}_{cr}$. If $\tilde{\ell}$ is smaller than $\widetilde{\mathrm{L}}_{cr}$, the waves never reach a group velocity matching V and propagate backward in the frame of the TC, until leaving the cyclone. The strongest waves at a given location are then the waves which originate from the $y = ax$ $(x > 0)$ segment. However, if $\tilde{l} > \widetilde{\mathrm{L}}_{cr}$, waves may reach V before exiting the cyclone. The optimal fetch configuration then corresponds to waves originating from the location $\widetilde{\mathrm{Y}} = \widetilde{\mathrm{L}}_{cr}$. They first travel backward in the frame of the TC, their group velocity increasing until reaching V at a so-called turning point ($\alpha = \alpha_T$) on the $y = -ax$ $(x > 0)$ segment, after traveling distance $\widetilde{\mathrm{L}}_{cr}$. Then they start to propagate forward increasing their group velocity ($\alpha < \alpha_T$) until leaving the TC. These waves have an extended fetch $\widetilde{\mathrm{Y}} + \widetilde{\mathrm{L}}_{cr}$.

Finally, in the left quadrant, where the TC propagation is opposite to the TC winds, the waves propagate backward and have a reduced fetch compared to the stationary case. In the left quadrant, the strongest waves are those who originate from the $y = -ax$ $(x < 0)$ segment.

In a cyclone moving at speed V, the inverse age α of the strongest waves at a given location can then be estimated by

$$\begin{cases} \alpha^{1/q}\left[1-(1+q)^{-1}\alpha/\alpha_T\right] = c_\alpha^{1/q}\left[\widetilde{\mathrm{Y}} - \widetilde{\mathrm{L}}_{cr}\right] & \text{if} \quad x > 0 \quad \text{and} \quad \tilde{\ell} > \widetilde{\mathrm{L}}_{cr}, \\ \alpha^{1/q}\left[1-(1+q)^{-1}\alpha/\alpha_T\right] = c_\alpha^{1/q}\left[\widetilde{\mathrm{Y}} - \tilde{\ell}\right] & \text{if} \quad x > 0 \quad \text{and} \quad \tilde{\ell} < \widetilde{\mathrm{L}}_{cr}, \\ \alpha^{1/q}\left[1+(1+q)^{-1}\alpha/\alpha_T\right] = c_\alpha^{1/q}\ \widetilde{\mathrm{Y}} & \text{if} \quad x < 0. \end{cases} \tag{7}$$

The energy $\widetilde{\mathrm{E}}$ is then deduced from Equation 7 through

$$\widetilde{\mathrm{E}} = c_e(\alpha/c_\alpha)^{p/q}. \tag{8}$$

It should be noted that Kudryavtsev et al. (2015) use Equations 5, 7, and 8 to estimate wave properties only on the $y = ax$ and $y = -ax$ segments, whereas in the following, they are used within the two quadrants of Sam.

In the KGC15 model, the TC forcing conditions (wind speed and propagation velocity) are supposed to be constant while the waves are propagating in the TC. The above relations are thus relevant if the TC is quasi-stationary during the time-period T, this yields an upper bound on the fetch duration

$$\mathrm{T} \leqslant \frac{u_w}{g}\frac{2c_\alpha}{1+q}\left(\tilde{\ell} + \widetilde{\mathrm{L}}_{cr}\right)^{1+q}. \tag{9}$$

For winds blowing at 40 m/s at a distance of 30 km from the TC axis in a cyclone moving at 5 m/s, Equation 9 provides 4.5 hr. Hence, the model assumes steady conditions (winds and translation velocity) over a period of the order of a few hours, which is in most cases a very reasonable assumption.

5.2. Extented Fetch in Sam

The observational data for SWH shown in Figure 3a are first compared to the SWH as predicted by the KGC15 model. For each observation, $\widetilde{\mathrm{Y}}$ is calculated from the location of the measurement, as well as the corresponding $\tilde{l}$. Both the surface wind measurement at the same location and the cyclone propagation speed at the time of

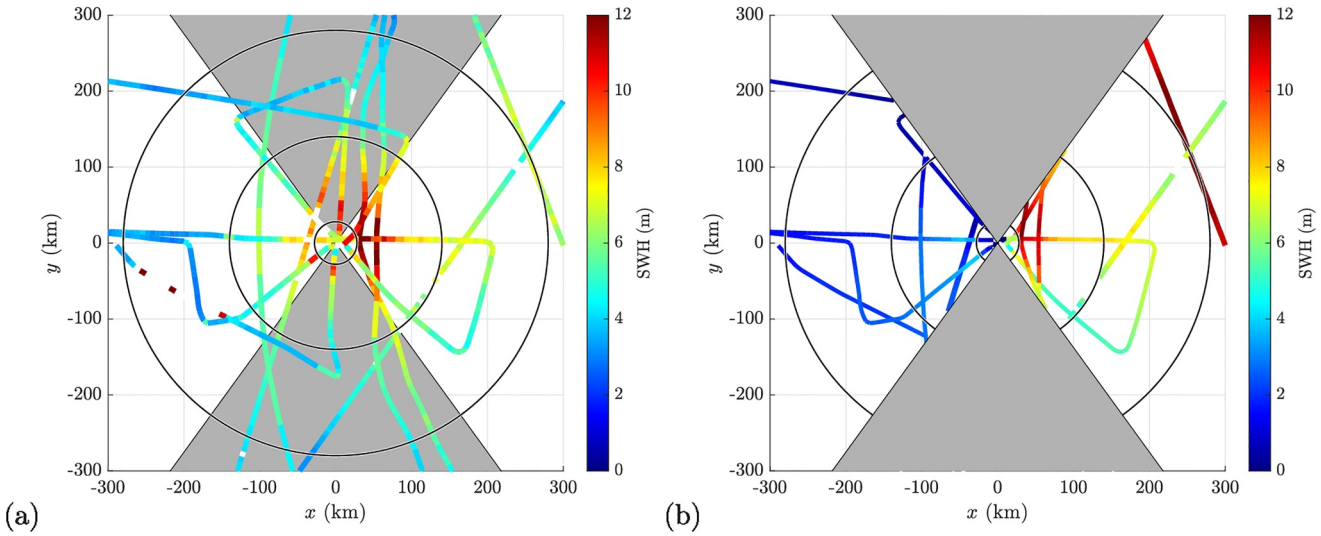

Figure 12. (a) Composite representation of SWH observational data between 29 September 00:00 and 2 October 12:00 reported in the frame of Hurricane Sam (the top of the figure corresponds to its propagation direction). The observations used to obtain this composite are the same as those listed in the caption of Figure 3. (b) SWH predicted by the KGC15 model. Shaded gray: area not described by the KGC15 model. Black circles indicate R_{max}, 5 R_{max}, and 10 R_{max}.

measurement estimated from the IBTrACS database, are used to estimate $\widetilde{L}_{cr}$. The SWH predicted by the model is then deduced from Equations 7 and 8. For the calculation of the modeled SWH in the case of buoys and saildrone, the surface wind speed provided by these two devices is used, whereas for satellite observations by SWIM and Sentinel 3-SRAL, the calculation relies on wind measurements from the CSCAT and the Sentinel 3-SRAL instruments, respectively. Finally, since aircraft observations do not include surface winds, ECMWF surface winds interpolated along the aircraft trajectory are being used in this case.

In order to facilitate the comparison, the SWH observations are reported in Figure 12a, whereas the SWH predicted by the KGC15 model are juxtaposed in Figure 12b. The figure is presented in the reference frame of the TC and orientated with the TC propagation direction upward. The locations outside the gray-shaded area represent the areas where, according to the KGC15 model, the wind can reasonably be assumed to be parallel to the TC propagation direction. In contrast, within the gray-shaded areas, the wind vectors are nearly orthogonal to the TC propagation, which definitely prevents the use of the KGC15 model.

It is important to keep in mind that the KGC15 model is based on simplifying assumptions, including winds and waves propagating along a direction parallel to the cyclone displacement, and a constant wind speed along this direction. Discrepancies between the model estimations and the observations are therefore inevitable.

The model reproduces the asymmetric wave field. In the right quadrant, the modeled SWH is globally consistent with the observed SWH, except on the SWIM track of 2 October, for which the model overestimates the SWH. This could be explained by the large distance of this track from the center of the cyclone (close to 10 R_{max}). Data available in the left quadrant are provided by CFOSAT (SWIM and CSCAT), buoy 41049 and the aircraft. For all these cases, the model underestimates the SWH in the left quadrant. While this could be due to an underestimation of wind speed, this is also the case for buoy 41049 with in situ wind measurements. This underestimation appears to be most likely related to simplifications inherent to the KGC15 model. Indeed, the model assumes that waves travel along a direction parallel to the TC displacement. In particular, in the model, no waves are radiated from the eyewall. Since the model predicts weak waves in this quadrant, it is likely that other waves than those described by the model are more energetic. This makes the model less suited to the left quadrant of the cyclone, where the observed angle between wind and wave is larger than in the right quadrant. As we will see, the KGC15 model can however efficiently be used to investigate the possible existence of trapped waves in the right quadrant.

We first focus on the data collected by the aircraft during its flight between 29 September 20:38 and 30 September 03:03. Its path is depicted in the frame of Sam in Figure 13, as well as a sample of the wave height spectra provided by the WSRA aboard the aircraft. We use here the SWH measured by the aircraft during its flight

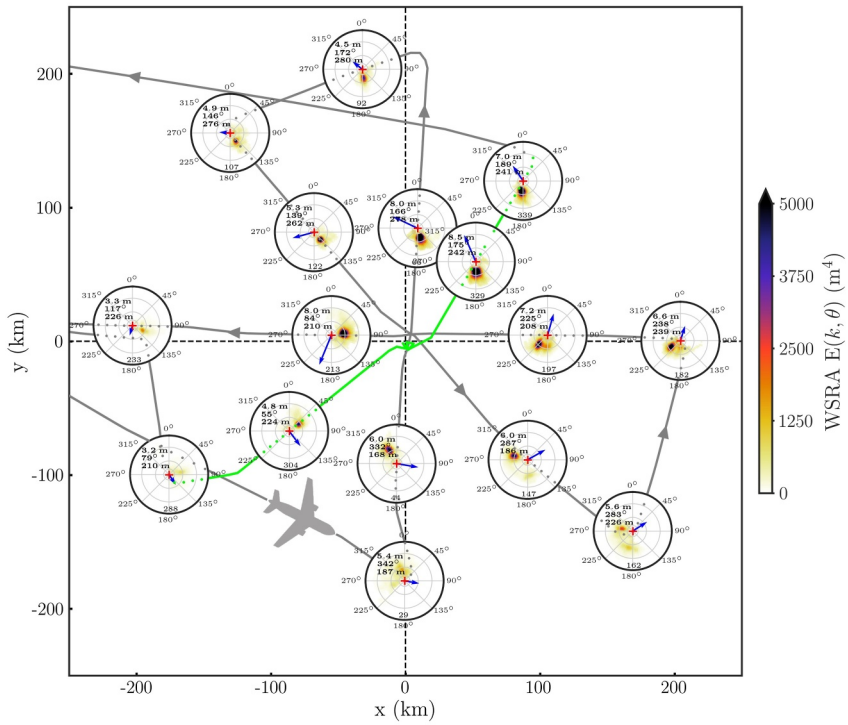

Figure 13. Reconnaissance flight (in gray) superimposed to a sample of the wave height spectra provided by the WSRA onboard the aircraft. The top of the figure, as well the 0° angle in spectra corresponds to the direction of propagation of Sam (spectra indicate the 'from' direction). Green color: data used in Figure 14. Blue arrows: ECMWF wind vectors interpolated at measurement location. The SWH, θ_p and λ_p are indicated in the top-left part of each spectra.

through the left-rear and right-front quadrants of Sam on 30 September between 01:16 and 02:09; the corresponding path is highlighted in green in Figure 13. This leg lies in the region of validity of the model, thanks to the choice of $a = 1.37$ highlighted above.

The SWH measured by the WSRA onboard the aircraft is then compared to the modeled SWH, calculated using Equation 8 and the ECMWF surface wind speed, U_{10}, interpolated along the aircraft trajectory (Figure 14a). The SWH profiles across Sam are shown in Figure 14b. If the TC is assumed to be stationary ($V = 0$), the SWH predicted by the KGC15 model strongly underestimates the SWH observed in the right-front sector (compare the black dots and the dashed line in Figure 14b), which suggests that the asymmetry of the wind alone can not explain the observed asymmetry in SWH. However, if a value of $V = 5$ m·s^{-1} as suggested by the IBTrACS information is used, the KGC15 model reproduces the large SWH observed in the right front sector. That means that a trapped wave mechanism can be invoked to explain the SWH asymmetry. It is however important to keep in mind that the ECMWF wind might underestimate winds in Sam (see the animation provided as Supporting Information S1 for the ECMWF winds superimposed to the in situ measurements in panel d).

We now turn to the in situ measurements (saildrone and buoy) in order to have collocated measurements of waves and wind at the surface. This KGC15 model thus finally tested in Figure 15 using the in situ measurements by the SD and buoy 41044. Indeed, these two instruments provide colocated measurements of wind and waves across the right quadrants of Sam, where the phenomenon of trapped waves is likely to occur. Buoy 41044 and the SD are located a few tens of kilometers away from the TC center when this latter passed over the area (see insets in Figures 15a and 15c). The surface wind speed and SWH measured by the SD from 29 September 01:00 to 1st October 17:30 (resp. by the buoy 41044 from 28 September 10:40 to 1st October 10:40) are shown in Figure 15a (resp. Figure 15c), as a function of the distance to the TC center, r, defined as positive in the right-front quadrant and negative in the right-rear quadrant. The SWH as estimated by the KGC15 model using the in situ wind profiles as well as the propagation velocity V of Sam (shown in Figures 15b and 15d) is superimposed in red in Figures 15a and 15c. Setting $V = 0$ in the model yields the black curve. In both cases, the latter strongly underestimates the SWH, whereas taking account the motion of Sam yields values much closer to the SWH

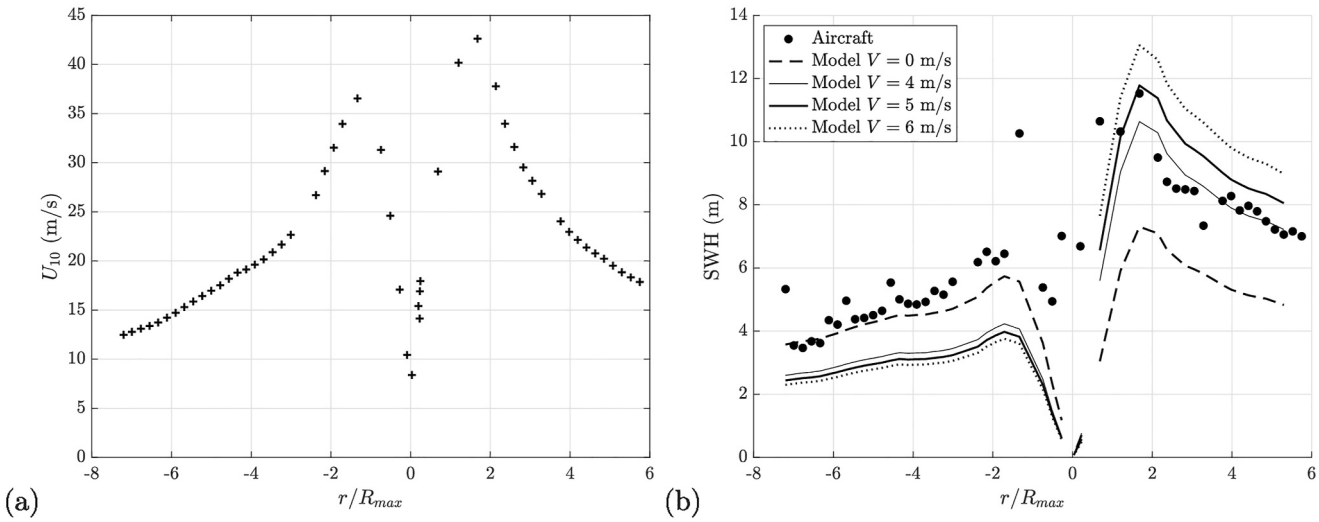

Figure 14. (a) ECMWF wind speed interpolated at the aircraft location, U_{10}. (b) SWH as measured by the aircraft (black dots) and estimated using the KGC15 model combined using U_{10} for $V = 0$ m·s^{-1} (dashed line), $V = 4$ m·s^{-1} (thin line), $V = 5$ m·s^{-1} (thick line) and $V = 6$ m·s^{-1} (dotted line). Abscissa: distance to the TC center (defined with the same sign as x) normalized by $R_{\max}$.

measurements. This implies that the large values of SWH observed in the right quadrants of Sam by the SD and by the buoy 41044 are consistent with the extended fetch theory.

The dimensional critical fetch L_{cr} for winds blowing at 40 m·s^{-1} and a translation velocity $V = 7$ m·s^{-1} (which is the value of V according to IBTrACS when both devices are closest to the center of Sam) is approximately 30 km. This corresponds to a distance of about 10 km from the axis. The SD and the buoy 41044 thus operate in regions where conditions are favorable for trapped waves.

To put this idea further to the test, the group velocity C_g is then calculated from the peak period T_p measured by both devices using the gravity waves dispersion relation. It is shown in Figures 15b and 15d (see the black diamonds). It can be noticed that the group velocity measured by the SD exhibits more variability than that measured by the buoy, this is due to fluctuations in the values of T_p.

In the KGC15 model, which involves a constant V, trapped waves are characterized by $C_g = V$ at the turning point, where waves change direction (from backward to forward), and by an increasing C_g as they propagate forward. This increasing C_g is consistent with a decreasing dominant wavelength, as measured by the SD and the buoy 41044 as Sam passes over these (Figure 3b). The propagation speed V of Sam during the time period investigated here keeps decreasing as r increases (see the black crosses in Figures 15b and 15d). In order to take this tendency into account, the ratio C_g/V is superimposed to the C_g and V profiles in Figures 15b and 15d (blue dots). The ratio C_g/V as measured by the SD (resp. by the buoy 41044) varies from 0.5 (resp. 1) to 2.5 as r increases, which is consistent with growing waves propagating forward. The region where C_g is approximately equal to V (compare the blue dots to the blue line indicating $C_g = V$ in Figures 15b and 15d) is located upstream of the region with the highest SWH (blue dots in Figures 15a and 15c), which is expected in the trapped wave phenomenon. The ratio C_g/V as predicted by the KGC15 model is superimposed (see the red curve in Figures 15b and 15d): it provides a good description of the C_g/V profile obtained from observations, which corroborates a wave trapping mechanism in the area explored by the SD and the buoy 41044.

6. Conclusions

We present a comprehensive study of extreme waves under Hurricane Sam (2021). We take advantage of the numerous observational data in this hurricane from satellite, aircraft and in situ instruments, to investigate the physics of waves.

Satellite observations under the heavy rain conditions of TCs are notoriously difficult. Whereas the SWIM wave measurements have been used in a few previous studies to investigate waves in tropical cyclones, the relevance of the wave spectra in such heavy rain conditions has not been investigated so far. In the present study, we assess the

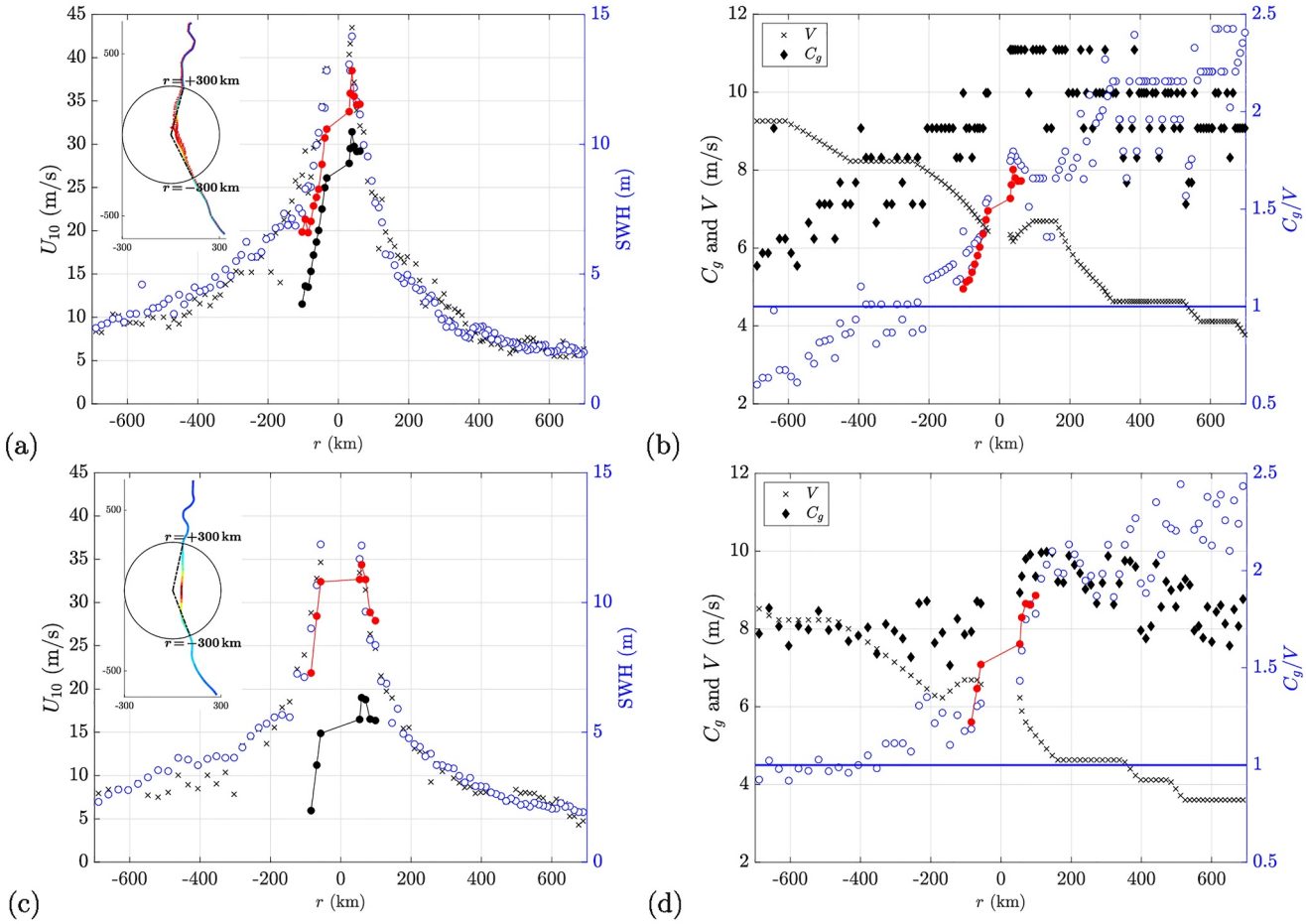

Figure 15. (a) Surface wind speed U_{10} (black crosses) and SWH measured by the SD (blue circles), superimposed to the SWH estimated by the KGC15 model using the translation velocity of Sam V (red line) or setting $V = 0$ m·s^{-1} (black line). Abscissa: distance to the TC center (negative values backward, positive values forward, as shown on the insets). (b) Group velocity C_g measured by the SD (black diamonds) and V (black crosses), superimposed to C_g/V (blue circles) and to its estimation by the KGC15 model (red line). Blue line indicates $C_g/V = 1$. Panels (c) and (d) same as (a) and (b) but for the buoy 41044. The trajectory in the frame of Sam of the SD and of the buoy 41044 (colored by the SWH and superimposed to the wind vectors) are shown on the insets in panels (a) and (c).

reliability of SWIM measurements in TCs, by comparing the SWIM wave spectra, as well as the averaged parameters (SWH, dominant wavelength, dominant direction), to that measured by 3 NDBC buoys and a saildrone (SD 1045) close to the track of Hurricane Sam. According to the spatial and temporal variability of waves in TCs, such a comparison makes sense only if the satellite and *situ* measurements are close enough, both in time and space, which strongly restricts the number of relevant comparisons. The case of Hurricane Sam, was thus complemented by 8 additional storms and hurricanes, for which collocated SWIM and NDBC measurements were performed in the vicinity of the storm, in various rain conditions, including heavy rain conditions. Those comparisons confirm the reliability of SWIM wave spectra, even in heavy rain conditions, despite a tendency for overestimating the energy at small k (more pronounced for SWH less than about 3 m) in the presence or absence of rain (Jiang et al., 2022). To understand why the SWIM spectra remain reliable in heavy rain conditions, we focused on the post-processing chain of the SWIM instrument, from the radar backscattering signal to the 2D wave spectra.

We have investigated the existence of trapped waves in Hurricane Sam, using a rare combination of satellite, aircraft and in situ wind and wave measurements. To do so, we also used the analytical model of Kudryavtsev et al. (2015) which predicts the wave properties (SWH and peak wavelength) in the right and left quadrants of a moving TC, given a surface wind speed profile. The model relies on the idea that, in the right quadrants of TCs, some waves may experience an extended fetch due to the displacement of the TC. This reinforces the SWH asymmetry induced by the wind speed asymmetry and results in the highest waves on the right of the

TC track in the Northern Hemisphere. Using the wind and wave measurements by a SD and a NDBC buoy through the right quadrants of Hurricane Sam, we have shown that a trapped wave mechanism can be invoked to explain the large SWH measured by both devices in the right-front quadrant. It is also consistent with the aircraft measurements complemented by ECMWF wind speed. The orientation and the distance of the SWIM tracks through Hurricane Sam were not optimal for comparisons with the model. The model to observations confrontation, also points to limitations of the Kudryavtsev et al. (2015) model to describe the wave field in the left quadrants of the cyclone.

Advances in observational technics for waves under tropical cyclones are impressive. Beside spectacular images and movies provided by saildrones in TCs, their wind and wave measurements can be very valuable to improve our understanding of the generation mechanisms of extreme waves in TCs. The same applies to the satellite wave measurements by SWIM, whose wave spectra have here been shown to be reliable even under heavy rain conditions. With more saildrones being deployed, and as SWIM continues to operate, more hurricanes will be sampled, opening the possibility for further studies using the combined approach advocated in this paper and will most certainly improve our understanding of the most threatening waves generated under a tropical cyclone.

Appendix A: SAR Performances

On 2 and 3 October 2021, the SWIM-CFOSAT and SAR-Sentinel1 instruments passed closed to each other (SWIM boxes and SAR imagettes being located at less than 40 km) in the rainbands of Sam with an approximate time-lapse of about 1h30. Figure A1 shows a first example of collocated SWIM and SAR wave height spectra on 2 October. Their locations are highlighted by the red and purple rectangles in Figure A1a, superimposed to the rain rate field: in this example no rain is detected within the SWIM box and the SAR imagette. The SAR SWH is a factor 1.5 smaller than the SWIM nadir SWH, and the SAR detects much less energy than SWIM at wavenumbers larger than 0.03 m^{-1} (i.e. wavelengths smaller than 160 m): this attenuation is characteristic of the cut-off effect. A second comparison, this time under moderate rain, is carried out in Figure A2. In this case, the rain rate reaches 3.4 mm/hr in the SWIM box and 3.2 mm/hr in the SAR imagette. The SAR SWH is smaller by a factor 2.5 compared to the SWIM nadir SWH and the SAR spectrum is strongly attenuated over the entire wavenumber range, compared to SWIM. Since the waves propagate in a direction closer to the range direction than to the azimuth direction, the cut-off effect can not explain such a discrepancy between both spectra and the latter is more likely due to rain.

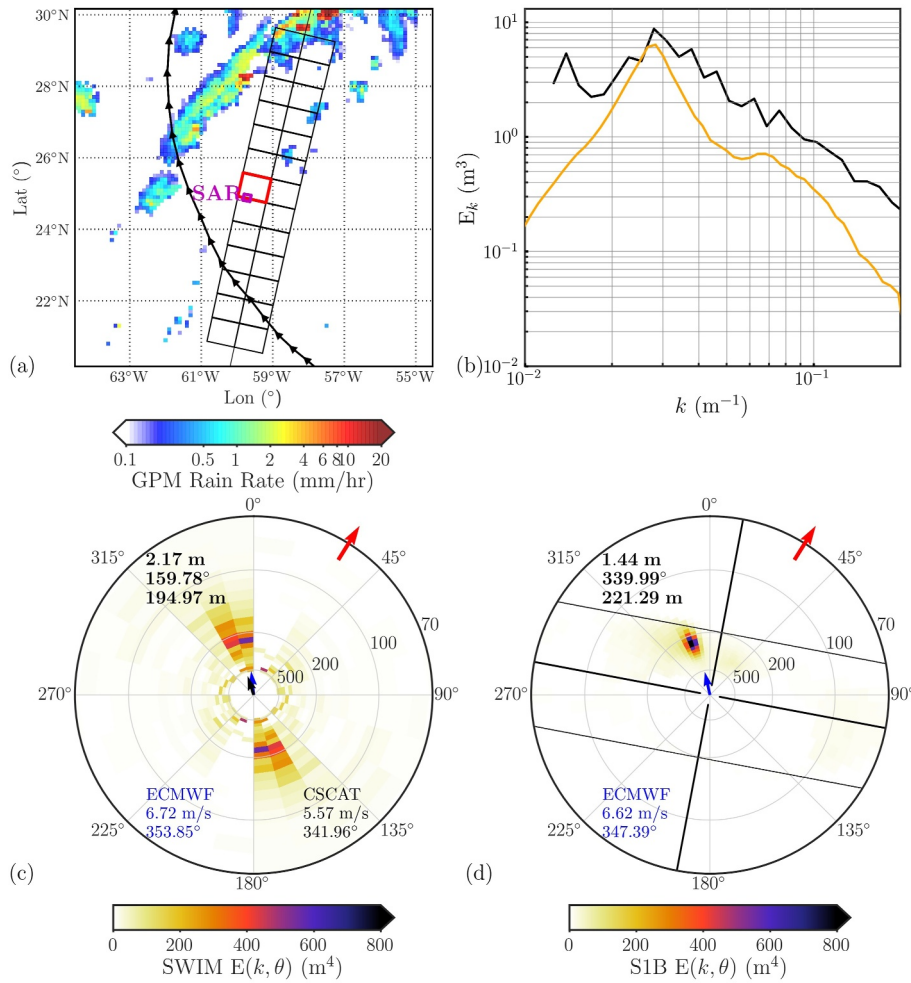

Figure A1. (a) SWIM boxes (black quadrangles) and SAR imagette (in purple) superimposed to the rain rate field in mm/hr (in colors); thick black line: the best track of the storm; cross: storm center during the passage of SWIM. (b) SWIM (black) and SAR (orange) 1D wave height spectra corresponding to the SWIM box highlighted in red in (a) and to the SAR imagette. Corresponding (c) SWIM and (d) SAR 2D wave height spectra; thick solid lines: azimuth and range directions, thin solid line: shortest detectable wavelengths. Black arrow: local wind vector from (c) CSCAT, blue arrows: ECMWF wind vectors. Red arrows on the outer circle of the spectra: propagation direction of Sam.

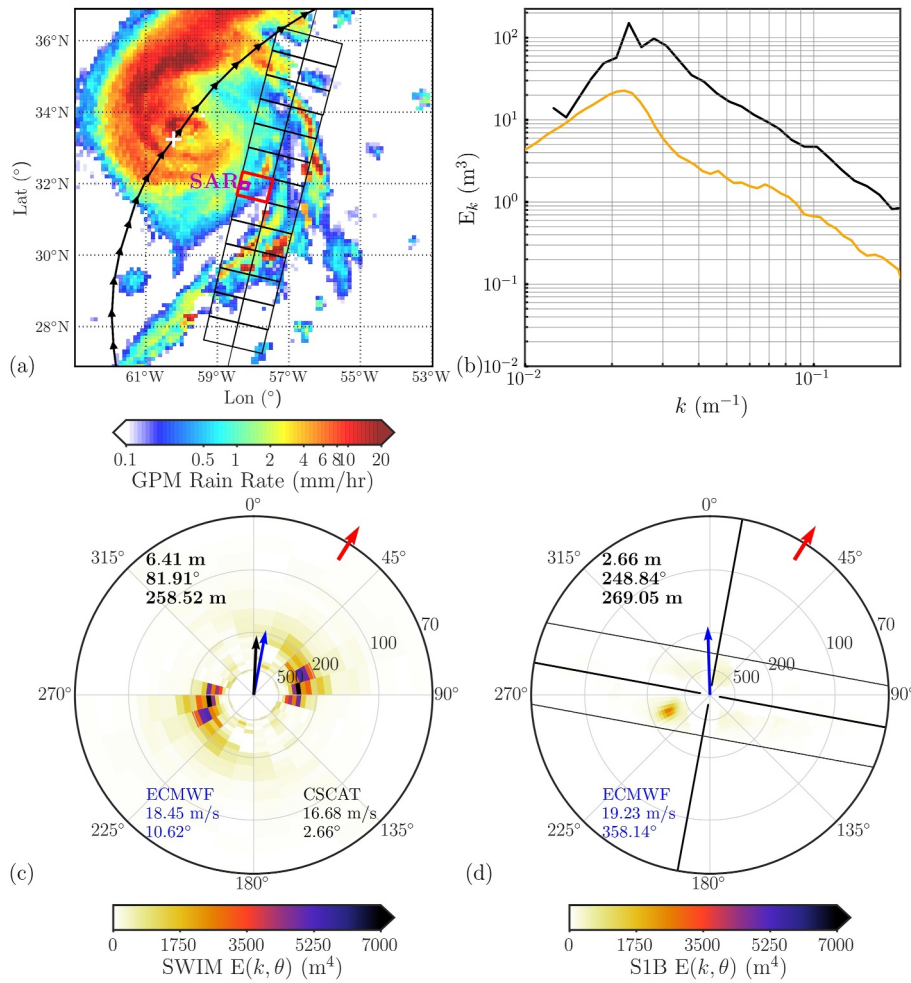

Figure A2. Same as Figure A1 but corresponding to SWIM boxes and SAR imagette under moderate rain conditions.

Appendix B: Statistical Study of the Rain Impact on Modulation Wave Spectra

Beyond the SWIM measurements along the 3 footprints shown in Figure 10, the measurements within the footprints within 350 km from the TC center during the passage of SWIM on 1st October 2021 are now investigated.

Figure B1 shows the averaged value of the reliable σ_0 profiles ($\overline{\sigma_0}$) as a function of the collocated rain rate (RR) estimated at the middle of the footprints, for the 3 spectral beams. It highlights the attenuation of $\overline{\sigma_0}$ by rain. For a RR of 10 mm/hr, it reaches up to 6 dB for the 10° beam. The spatial resolution of the IMERG product (about 10 km) is unfortunately too low for quantifying the rain inhomogeneities along the footprints (about 20 km length). The following figures thus involve the rain rate at the middle of the footprints. Figure B2a shows the large-scale variability of σ_0 within the footprints of the 10° spectral beam (quantified by the *lsvar* parameter) as a function of the rain rate RR. For moderate and heavy rains, there is a correlation between *lsvar* and RR. The representation of the averaged value of *lsvar* per rain rate category in Figure B2c corroborates the correlation between both quantities when RR is larger than 7 mm/hr. The energy of the small k peak on the modulation spectra is quantified by

$$\mathcal{E}_{k<k_c} = \int_{k<k_c} \mathrm{Pm}(k)dk, \tag{B1}$$

where $k_c = 2\pi \cdot 10^{-3}$ m^{-1} (i.e., $\lambda_c = 1$ km). This quantity corresponds to the energy of the modulation spectra at wavelengths larger than 1 km. This threshold value was chosen in order to distinguish the small k anomalous peak to the ocean wave spectrum. The energy of the rest of the modulation spectra (for $k > k_c$) is quantified by $\mathcal{E}_{k>k_c}$ defined in a similar way to (B1) but with $k > k_c$. Figure B2b shows $\mathcal{E}_{k<k_c}$ as a function of RR, whereas its averaged value per rain rate category is represented in Figure B2d. These figures highlight the correlation of $\mathcal{E}_{k<k_c}$ with RR for moderate and heavy rains. Actually, the rain rate at the middle of the footprint is not necessarily correlated to the rain inhomogeneities along the footprint. For example, the rain rate in Case 3 (third row in Figure 10) is larger than that in Case 2 (second row in Figure 10). Yet, the σ_0 signal is more distorted in Case 2, suggesting that rain inhomogeneities are more important in Case 2. This can explain why the correlations shown in Figure B2 are not stronger. The rain product spatial resolution (about 10 km) is definitely a limiting factor in the investigation of the impact of rain inhomogeneities on SWIM measurements. This is also the case for its half-hourly temporal resolution.

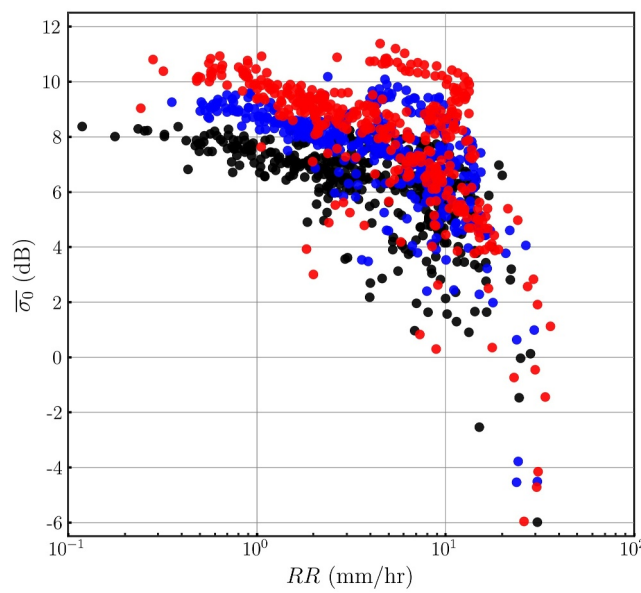

Figure B1. Averaged value of the reliable σ_0 profile ($\overline{\sigma_0}$) as a function of the collocated rain rate (RR) estimated at the middle of the 405 footprints of the 6° beam (red dots) and 407 footprints of the 8° (blue dots) and 10° (black dots) beams.

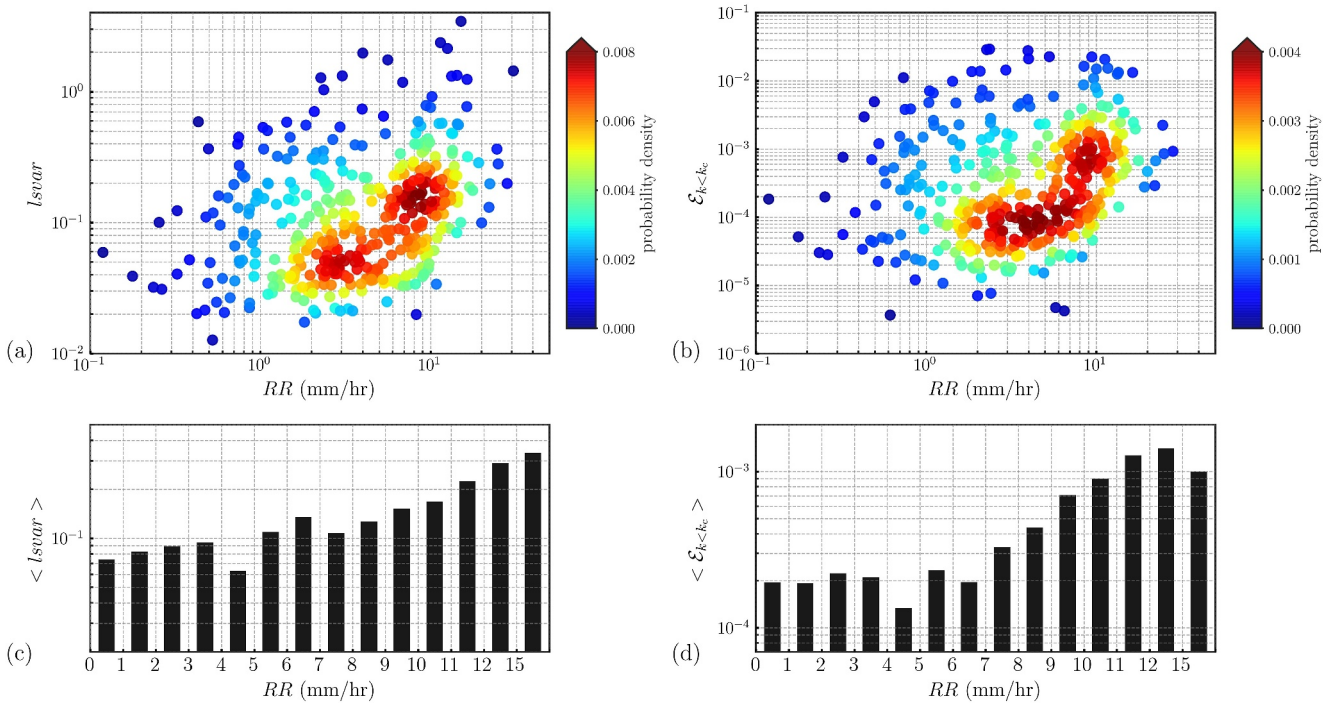

Figure B2. Scatterplot and probability density function (colors) of (a) the large-scale variability within the footprints (*lsvar*) and of (b) the energy $\mathcal{E}_{k<k_c}$, as a function of the rain rate *RR* at the middle of the 407 footprints of the 10° spectral beam. Corresponding averaged values of (c) *lsvar* and of (d) $\mathcal{E}_{k<k_c}$ per category of *RR*.

The investigation of the rain impact on the rest of the modulation spectrum (i.e., for $k > k_c$), including the waves energy, deserves a slightly different methodology, relying on both 8° and 10° spectral beams. Indeed, since this part of the modulation spectrum contains the waves energy, the rain impact can be assessed only by comparing measurements of the same waves but in different rain conditions. The idea is to compare modulation spectra derived from 8° to 10° beams corresponding to very close azimuth directions, thus measuring waves propagating in the same direction. Assuming that the distance between both footprints is smaller than the spatial variability of waves, but is larger than the spatial variability of the rain field, the discrepancy between both

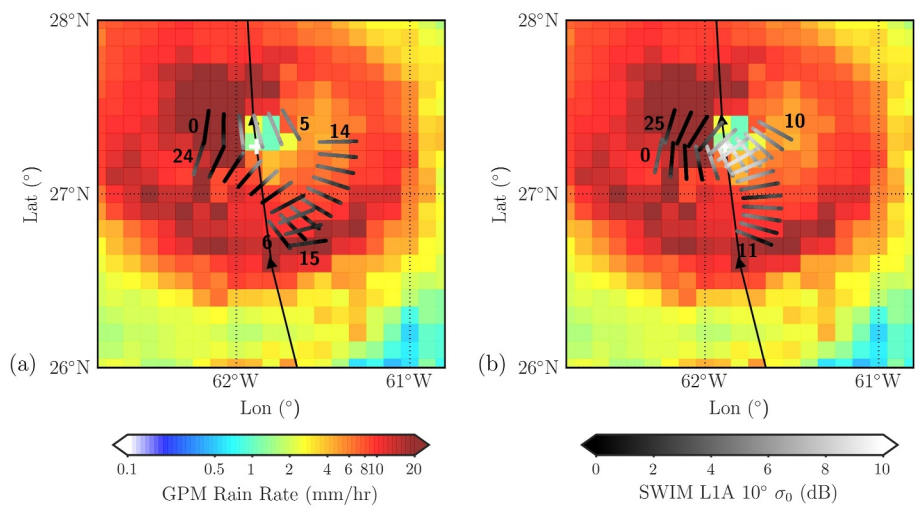

Figure B3. Footprints corresponding to the (a) 10° and (b) 8° beams, in box 78-1, superimposed to the rain rate field (in colors) on 1st October 11:30. Thick black line: trajectory of the center of Sam. White cross: location of the center of Sam during the passage of SWIM.

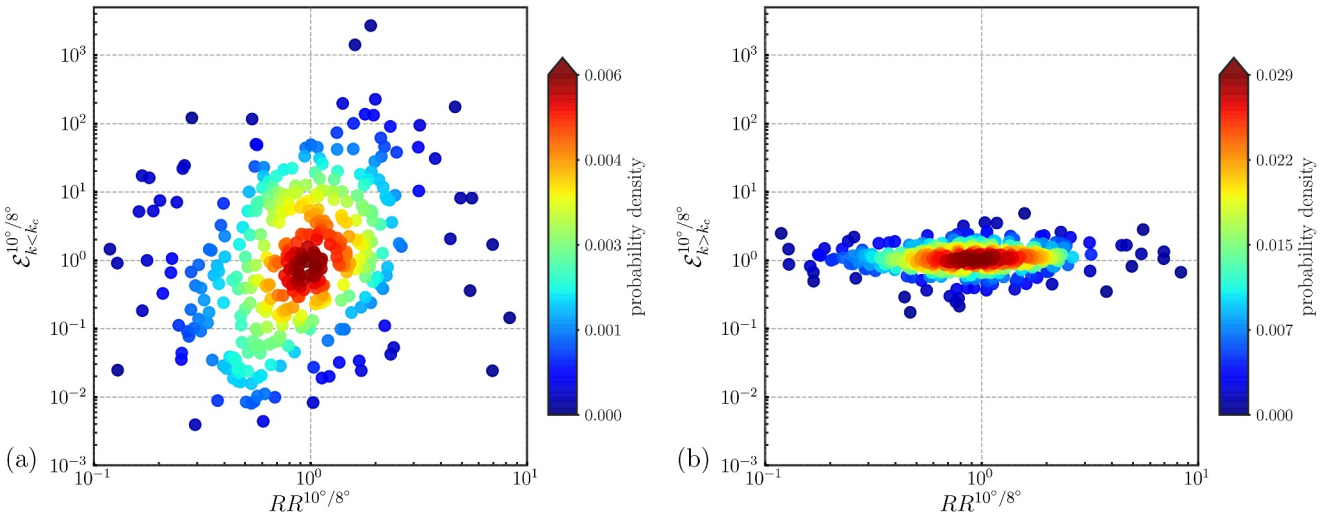

Figure B4. Scatterplot and probability density function (colors) of (a) $\mathcal{E}^{10/8^\circ}_{k<k_c}$ and (b) $\mathcal{E}^{10/8^\circ}_{k>k_c}$ as a function of $RR^{10/8^\circ}$, for 391 comparisons.

measurements can be assumed to be due to the rain impact. As an example, the footprints of the 10° beam (resp. 8° beam) corresponding to box 78-1 are superimposed to the rain rate field in Figure B3a (resp. B3b): whereas they are 22 km apart, the footprint number 3 of beam 10° in the azimuth direction 166° (Figure B3a) undergoes less rain ($RR \approx 2$ mm/hr) than the footprint number 4 of beam 8° in the very close azimuth direction 163° ($RR > 7$ mm/hr).

A comparison of the modulation spectra as measured within footprints corresponding to 10° and 8° beams in very close azimuth directions was undertaken, related to the rain rates. Among the 391 comparisons, the distance between both footprints varies from 20 to 53 km and the azimuth direction difference from 1.15° to 4.30°. Note that this methodology implies an estimation of rain at the middle of both footprints: hence, the limitations due to the spatial and temporal resolutions of the rain product are now twice as critical compared to Figure B2. Figure B4a shows the ratio of $\mathcal{E}_{k<k_c}$ measured at 10° to that at 8° (such a ratio is denoted as $\mathcal{E}^{10/8^\circ}_{k<k_c}$), as a function of the ratio of rain rates, denoted as $RR^{10/8^\circ}$. Despite scattered data, this figure exhibits a correlation between both quantities, which is consistent with Figure B2b. Such a correlation is not observed between $\mathcal{E}^{10/8^\circ}_{k>k_c}$ and $RR^{10/8^\circ}$, as shown in Figure B4b. This suggests that rain mainly impacts the modulation spectra at small wavenumbers ($k < k_c$), rather than the waves range.

Data Availability Statement

The CFOSAT SWIM data are available on https://aviso-data-center.cnes.fr (L1A) and https://www.aviso.altimetry.fr/en/data/products/wind/wave-products/wave-wind-cfosat-products.html (L1B and L2). The SWIM L2S data are provided by the Ifremer Wind and Wave Operation Center on https://cersat.ifremer.fr/fr/Projects/Recent-and-ongoing-projects/IWWOC. The in situ data are available on the NOAA website: https://data.pmel.noaa.gov/pmel/erddap/tabledap/sd1045_hurricane_2021.html and https://www.ndbc.noaa.gov. The IBTrACS database can be downloaded from https://www.ncei.noaa.gov/data/international-best-track-archive-for-climate-stewardship-ibtracs/v04r00. The ECMWF wind data are available on the ECMWF's Meteorological Archival and Retrieval System (https://confluence.ecmwf.int/display/CEMS/MARS). Finally, the GPM IMERG precipitation data can be downloaded from NASA https://gpm.nasa.gov/data/directory.

Acknowledgments
This work was performed during a research visit of Xiaolu Zhao in Sorbonne Université from April 2022 to April 2024. This work was supported in part by the China Scholarship Council (CSC) Ph.D. Joint Training Program under Grant 202109040021 and by the National Natural Science Foundation under Grant 42076181. This research project is partly supported by the CNES/TOSCA (Maeva project). We thank the NOAA and the Saildrone company for sharing the saildrone data. We are grateful to two anonymous referees for their help in improving our article.

References

Alpers, W., Zhang, B., Mouche, A., Zeng, K., & Chan, P. W. (2016). Rain footprints on c-band synthetic aperture radar images of the ocean - Revisited. *Remote Sensing of Environment*, *187*, 169–185. https://doi.org/10.1016/j.rse.2016.10.015

Badulin, S. I., Babanin, A. V., Zakharov, V. E., & Resio, D. (2007). Weakly turbulent laws of wind-wave growth. *Journal of Fluid Mechanics*, *591*, 339–378. https://doi.org/10.1017/s0022112007008282

Bidlot, J.-R., Prates, F., Ribas, R., Mueller-Quintino, A., Crepulja, M., & Vitart, F. (2020). Enhancing tropical cyclone wind forecasts. *ECMWF Newsletter*, *164*, 33–37.

Bowyer, P., & MacAfee, A. W. (2005). The theory of trapped-fetch waves with tropical cyclonesan operational perspective. *Weather and Forecasting*, *20*(3), 229–244. https://doi.org/10.1175/waf849.1

Cavaleri, L., Bertotti, L., & Bidlot, J.-R. (2015). Waving in the rain. *Journal of Geophysical Research: Oceans*, *120*(5), 3248–3260. https://doi.org/10.1002/2014jc010348

Cline, I. M. (1920). Relation of changes in storm tides on the coast of the Gulf of Mexico to the center and movement of hurricanes. *Monthly Weather Review*, *48*(3), 127–146. https://doi.org/10.1175/1520-0493(1920)48<127:rocist>2.0.co;2

Earle, M. D. (2003). *Nondirectional and directional wave data analysis procedures (Tech. Rep.)*. U.S. National Oceanic and Atmospheric Administration, National Data Buoy Center. Available on-line at: http://www.ndbc.noaa.gov/wavemeas.pdf

Hauser, D., Abdalla, S., Ardhuin, F., Bidlot, J.-R., Bourassa, M., Cotton, D., et al. (2023). Satellite remote sensing of surface winds, waves, and currents: Where are we now? *Surveys in Geophysics*, *44*(5), 1357–1446. https://doi.org/10.1007/s10712-023-09771-2

Hauser, D., Tourain, C., Hermozo, L., Alraddawi, D., Aouf, L., Chapron, B., et al. (2021). New observations from the swim radar on board CFOSAT: Instrument validation and ocean wave measurement assessment. *IEEE Transactions on Geoscience and Remote Sensing*, *1*, 05–26. https://doi.org/10.1109/tgrs.2020.2994372

Huffman, G., Stocker, E., Bolvin, D. T., Nelkin, E. J., & Tan, J. (2023). *GPM IMERG final precipitation L3 half hourly 0.1 degree x 0.1 degree v07*. Goddard Earth Sciences Data and Information Services Center (GES DISC). https://doi.org/10.5067/GPM/IMERG/3B-HH/07

Hwang, P. A., Wang, D. W., Walsh, E. J., Krabill, W. B., & Swift, R. N. (2000). Airborne measurements of the wavenumber spectra of ocean surface waves. Part I: Spectral slope and dimensionless spectral coefficient. *Journal of Physical Oceanography*, *30*(11), 2753–2767. https://doi.org/10.1175/1520-0485(2001)031<2753:amotws>2.0.co;2

Jiang, H., Song, Y., Mironov, A., Yang, Z., Xu, Y., & Liu, J. (2022). Accurate mean wave period from SWIM instrument on-board CFOSAT. *Remote Sensing of Environment*, *280*, 113149. https://doi.org/10.1016/j.rse.2022.113149

King, D. B., & Shemdin, O. H. (1978). Radar observations of hurricane wave directions. In *Proc., 16th international confession on coastal engineering; Hamburg, West Germany* (pp. 209–226).

Knapp, K. R., Kruk, M. C., Levinson, D. H., Diamond, H. J., & Neumann, C. J. (2010). The international best track archive for climate stewardship (IBTRACS). *Bulletin America Meteorology Social*, *91*(3), 363–376. https://doi.org/10.1175/2009bams2755.1

Kudryavtsev, V., Golubkin, P., & Chapron, B. (2015). A simplified wave enhancement criterion for moving extreme events. *Journal of Geophysical Research: Oceans*, *120*(11), 7538–7558. https://doi.org/10.1002/2015jc011284

Kudryavtsev, V., Yurovskaya, M., & Chapron, B. (2021a). 2D parametric model for surface wave development under varying wind field in space and time. *Journal of Geophysical Research: Oceans*, *126*(4), e2020JC016915. https://doi.org/10.1029/2020jc016915

Kudryavtsev, V., Yurovskaya, M., & Chapron, B. (2021b). Self-similarity of surface wave developments under tropical cyclones. *Journal of Geophysical Research: Oceans*, *126*(4), e2020JC016916. https://doi.org/10.1029/2020jc016916

Kudryavtsev, V., Yurovskaya, M., Chapron, B., Collard, F., & Donlon, C. (2017). Sun glitter imagery of ocean surface waves. Part 1: Directional spectrum retrieval and validation. *Journal of Geophysical Research: Oceans*, *122*(2), 1369–1383. https://doi.org/10.1002/2016jc012425

Lehner, S., Pleskachevsky, A., & Bruck, M. (2012). High-resolution satellite measurements of coastal wind field and sea state. *International Journal of Remote Sensing*, *33*(23), 7337–7360. https://doi.org/10.1080/01431161.2012.685975

Le Merle, E., Hauser, D., & Yang, C. (2022). Wave field properties in tropical cyclones from the 2 spectral observation of the CFOSAT/SWIM. *Geophysical Research Letters*, *128*, e2022JC019074. https://doi.org/10.1029/2022JC019074

Li, D., Staneva, J., Bidlot, J.-R., Grayek, S., Zhu, Y., & Yin, B. (2021). Improving regional model skills during typhoon events: A case study for super typhoon lingling over the northwest Pacific Ocean. *Frontiers in Marine Science*, *8*, 613913. https://doi.org/10.3389/fmars.2021.613913

Lygre, A., & Krogstad, H. E. (1986). Maximum entropy estimation of the directional distribution in ocean wave spectra. *Journal of Physical Oceanography*, *16*(12), 2052–2060. https://doi.org/10.1175/1520-0485(1986)016<2052:meeotd>2.0.co;2

Oruba, L., Hauser, D., Planes, S., & Dormy, E. (2022). Ocean waves in the south pacific: Complementarity of SWIM and SAR observations. *Earth and Space Science*, *9*(6). https://doi.org/10.1029/2021ea002187

Ponce de León, S., & Bettencourt, J. (2021). Composite analysis of North Atlantic extra-tropical cyclone waves from satellite altimetry observations. *Advances in Space Research*, *68*(2), 762–772. https://doi.org/10.1016/j.asr.2019.07.021

Popstefanija, I., Fairall, C. W., & Walsh, E. J. (2021). Mapping of directional ocean wave spectra in hurricanes and other environments. *IEEE Transactions on Geoscience and Remote Sensing*, *59*(11), 9007–9020. https://doi.org/10.1109/tgrs.2020.3042904

Quilfen, Y., Chapron, B., & Tournadre, J. (2010). Satellite microwave surface observations in tropical cyclones. *Monthly Weather Review*, *111*, C01004.

Quilfen, Y., Tournadre, J., & Chapron, B. (2006). Altimeter dual-frequency observations of surface winds, waves, and rain rate in tropical cyclone Isabel. *Journal of Geophysical Research*, *111*(C1), C01004. https://doi.org/10.1029/2005jc003068

Ricciardulli, L., Foltz, G., Manaster, A., & Meissner, T. (2022). Assessment of saildrone extreme wind measurements in hurricane SAM using MW satellite sensors. *Remote Sensing*, *14*(12), 2726. https://doi.org/10.3390/rs14122726

Shi, Y., Du, Y., Chu, X., Tang, S., Shi, P., & Jiang, X. (2021). Asymmetric wave distributions of tropical cyclones based on CFOSAT observations. *Journal of Geophysical Research: Oceans*, *126*(4), e2020JC016829. https://doi.org/10.1029/2020jc016829

Sun, F., Yang, J., & Cui, W. (2024). Accuracy evaluation of ocean wave spectra from sentinel-1 SAR based on buoy observations and ERA5 data. *Remote Sensing*, *16*(987), 987. https://doi.org/10.3390/rs16060987

Tannehill, I. R. (1936). Sea swells in relation to movement and intensity of tropical cyclones. *Monthly Weather Review*, *64*, 231–236.

Tournadre, J., Lambin-Artru, J., & Steunou, N. (2009). Cloud and rain effects on ALTIKA/SARAL Ka-band radar altimeter—Part I: Modeling and mean annual data availability. *IEEE Transactions on Geoscience and Remote Sensing*, *47*(6), 1806–1817. https://doi.org/10.1109/tgrs.2008.2010130

Welch, P. D. (1967). The use of fast fourier transforms for the estimation of power spectra: A method based on time averaging over short modified periodograms. *IEEE Transactions on Audio and Electroacoustics*, *15*(2), 70–73. https://doi.org/10.1109/tau.1967.1161901

Xiang, K., Yin, X., Xing, S., Kong, F., Li, Y., Lang, S., & Gao, Z. (2022). Preliminary estimate of CFOSAT satellite products in tropical cyclones. *IEEE Transactions on Geoscience and Remote Sensing*, *60*, 4203516. https://doi.org/10.1109/tgrs.2021.3103277

Xu, Y., Hauser, D., Liu, J., Si, J., Yan, C., Chen, S., et al. (2022). Statistical comparison of ocean wave directional spectra derived from SWIM/CFOSAT satellite observations and from buoy observations. *IEEE Transactions on Geoscience and Remote Sensing*, *60*, 1–20. https://doi.org/10.1109/tgrs.2022.3199393

Young, I. R. (1988). Parametric hurricane wave prediction model. *Journal of Waterway, Port, Coastal, and Ocean Engineering*, *114*(5), 637–652. https://doi.org/10.1061/(asce)0733-950x(1988)114:5(637)

Young, I. R. (2017). A review of parametric descriptions of tropical cyclone wind-wave generation. *Atmosphere*, *8*(194), 1–20. https://doi.org/10.3390/atmos8100194

Yurovskaya, M., Kudryavtsev, V., Mironov, A., Mouche, A., Collard, F., & Chapron, B. (2022). Surface wave developments under tropical cyclone Goni (2020): Multi-satellite observations and parametric model comparisons. *Remote Sensing*, *14*(9), 2032. https://doi.org/10.3390/rs14092032

Zhao, X., Lin, W., Portabella, M., Wang, Z., & He, Y. (2022). Effects of rain on CFOSAT scatterometer measurements. *Remote Sensing of Environment*, *274*, 113015. https://doi.org/10.1016/j.rse.2022.113015

Zhao, X., Shao, W., Zhao, L., Gao, Y., Hub, Y. Y., & Yuan, X. (2021). Impact of rain on wave retrieval from sentinel-1 synthetic aperture radar images in tropical cyclones. *Advances in Space Research*, *67*(10), 3072–3086. https://doi.org/10.1016/j.asr.2021.01.050

Zieger, S., Inoth, J. V., & Young, I. R. (2009). Joint calibration of multiplatform altimeter measurements of wind speed and wave height over the past 20 years. *Journal of Atmospheric and Oceanic Technology*, *26*(12), 2549–2564. https://doi.org/10.1175/2009jtecha1303.1